SLAC–PUB–5934
October 1992
(T/E)

MEASUREMENTS OF TRANSVERSE ELECTRON SCATTERING FROM THE DEUTERON IN THE THRESHOLD REGION AT HIGH MOMENTUM TRANSFERS*

M. FRODYMA,(2,a) R. G. ARNOLD,(1) D. BENTON,(1,b) P. E. BOSTED,(1) L. CLOGHER,(1) G. DECHAMBRIER,(1) A. T. KATRAMATOU,(1) J. LAMBERT,(1,c) A. LUNG,(1), G. G. PETRATOS,(1,d) A. RAHBAR,(1) S. E. ROCK,(1) Z. M. SZALATA,(1) B. DEBEBE,(2) R. S. HICKS,(2) A. HOTTA,(2,e) G. A. PETERSON,(2) R. A. GEARHART,(3) J. ALSTER,(4) J. LICHTENSTADT,(4) F. DIETRICH,(5) AND K. VAN BIBBER(5)

(1) *The American University, Washington, D.C. 20016*
(2) *University of Massachusetts, Amherst, Massachusetts 01003*
(3) *Stanford Linear Accelerator Center, Stanford, California 94309*
(4) *Tel Aviv University, Tel Aviv, Israel*
(5) *Lawrence Livermore National Laboratory, Livermore, CA 94550*

Submitted to Physical Review C

---

*Work supported in part by Department of Energy contracts DE–AC03–76SF00515 (SLAC), W–7405–ENG–48 (LLNL), DE–AC02–76ER–02853 (U. Mass.); National Science Foundation Grant PHY85–10549 (A.U.); the U.S.–Israel Binational Science Foundation (Tel–Aviv); and the Monbusho International Research Program.

ABSTRACT

Deuteron electrodisintegration cross sections near 180° have been measured near break-up threshold for the four-momentum transfer squared Q^2 range 1.21 to 2.76 $(\mathrm{GeV/c})^2$. Evidence for a change of slope in the cross section near $Q^2 = 1$ $(\mathrm{GeV/c})^2$ has been obtained for the first time. The data are compared to non-relativistic calculations, which predict a strong influence of meson exchange currents. The data are also compared to a hybrid quark-hadron model. None of these calculations agrees with the data over the entire measured range of Q^2.

The ratio of inelastic structure functions $W_1(Q^2, E_{np})/W_2(Q^2, E_{np})$ is extracted from the present results and previous forward angle data. No prediction is in good agreement with the deduced ratios at small relative energy E_{np}.

I. INTRODUCTION

The electrodisintegration of the deuteron near breakup threshold provides one of the most compelling tests of our understanding of the role of meson exchange currents in nuclei. Close to threshold, the dominant mechanism for electrodisintegration is by a spin-flip magnetic dipole transition from the $^3S_1 +^3 D_1$ ground state to an unbound $^1S_0$ state, a transition that can be most selectively studied by electron scattering at extreme backward angles. This paper presents the results of measurements of the threshold electrodisintegration cross section at 180°, in the region where the relative kinetic energy E_{np} of the outgoing nucleons in the center-of-mass system is less than 20 MeV. Previous measurements [1] of this cross section extended to a squared four-momentum transfer $Q^2 = 1.1$ (GeV/c)^2. Our data span the range from $Q^2 = 1.21$ to 2.76 (GeV/c)^2, a region where the meson-exchange representation of the nucleon-nucleon force is expected to have diminishing applicability. The results presented here have been previous published [2]. This paper describes the experiment in more complete detail, particularly with regard to the procedures employed for extracting the average threshold cross sections. Additional information is provided on a comparison of $W_1(Q^2, E_{np})$, measured in the present experiment, with values of $W_2(Q^2, E_{np})$ from other experiments.

The one-photon exchange impulse approximation (IA) diagram is shown in Fig. 1 with and without final state interactions (FSI) between the two nucleons. Calculations in the IA predict a diffraction minimum at four momentum transfer squared $Q^2 \approx 0.5$ (GeV/c)^2, in strong disagreement with existing electrodisintegration data [1].

Significant improvement is found when meson-exchange currents (MEC) are included. Three important MEC interactions involving pions are shown in Fig. 2.

Non-relativistic predictions including only single pion MEC account [3] for the discrepancy at $Q^2 \approx 0.5$, but are inadequate at higher Q^2, where short-range effects exert a large influence. Above $Q^2 \approx 1$ (GeV/c)^2, non-relativistic predictions have a large model dependence, yielding order-of-magnitude variations in the calculated cross sections. The electromagnetic form factors used in the meson-nucleon coupling of the MEC contribute strongly to this model dependence. Whether calculations should use the Sachs $G_E(Q^2)$ or the Dirac $F_1(Q^2)$ form factor has been an issue of some debate [4,5,6]. Because previous data [1] were better described by models using F_1, theoretical arguments were advanced [5] in favor of F_1. Subsequently, it was shown [4,6] that these arguments depend on strong, unproven assumptions and in some cases have inconsistencies.

Other sources of uncertainty are the nucleon-nucleon (nn) potential [7,8], the πNN vertex form factors, and the nucleon electromagnetic form factors. More accurate measurements [9] of the neutron electric form factor $G_{En}(Q^2)$ have recently become available, substantially reducing this last source of uncertainty.

The strong model dependence at high Q^2 has led to an unsatisfactory situation. There appear to be several plausible combinations of theoretical inputs [4], but none of these is in good agreement with all electrodisintegration data for $Q^2 \leq 2.76$ (GeV/c)^2. Such observations underscore the need for a completely relativistic theory in which the number of *ad hoc* choices is minimized.

Another class of predictions for deuteron electrodisintegration are exploratory investigations [10,11,12] known as hybrid quark-hadron models. In these models the deuteron is treated as a six-quark cluster when the NN separation is less than a cut-off radius. Unfortunately, the models are quite sensitive to the value of the radius, which is not strongly constrained. These models also yield order-of-magnitude variations in the predicted cross sections at high Q^2.

This paper is organized as follows. Relevant kinematic and cross section formulae are given in Section II. Since the experimental apparatus has been discussed elsewhere, only a brief overview will be given in Section III. The main steps of the data analysis are discussed in Section IV. A comparison of the electrodisintegration data with several non-relativistic predictions is given in Section V, and concluding remarks are given in Section VI.

II. KINEMATICS and CROSS SECTIONS

In the formulas of this section the electron rest mass is neglected. The four-momentum transfer squared Q^2 is given by

$$Q^2 = 4EE' \sin^2(\theta/2) \ , \tag{1}$$

where E and E' are the incident and scattered electron energies, and θ is the electron scattering angle in the laboratory system. The invariant mass squared W^2 of the two-nucleon recoil system in Fig. 1 can be written as

$$W^2 = M_D^2 + 2M_D\nu - Q^2 \ , \tag{2}$$

where M_D is the deuteron mass, and $\nu = E - E'$.

For elastic scattering, $W^2 = M_D^2$ and $Q^2 = 2M_D\nu$. The scaling variable x_D is given by

$$x_D = \frac{Q^2}{2M_D\nu} \ , \tag{3}$$

which is near unity for threshold-inelastic data. A related scaling variable [13] ω' can be written as

$$\omega' = 1 + \frac{W_N^2}{Q^2} , \tag{4}$$

where W_N^2 is obtained by substituting the nucleon mass M_N in Eq. (2) for the deuteron mass. Both x_D and ω' are used in the data analysis discussed below.

In the threshold inelastic region, the excitation energy ω is small compared to the deuteron mass and is given by $\omega = W - M_D$. The scattered electron energy is given to first order in ω/M_D by

$$E' = \frac{E-\omega}{R_E}, \tag{5}$$

where

$$R_E = 1 + \frac{2E\sin^2(\theta/2)}{M_D} \tag{6}$$

is the recoil factor.

The electron spectrometer central momentum was set at the deuteron elastic peak for the threshold inelastic data taking. It is useful to express E' in terms of the momentum shift δ relative to the deuteron elastic peak as

$$E' = \frac{E}{R_E}(1+\delta) \ . \tag{7}$$

The kinetic energy E_{np} of an outgoing nucleon in the neutron-proton rest frame is given to first order in $\frac{\omega}{M_D}$ by

$$E_{np} = \omega - \omega_o \ , \tag{8}$$

or in terms of E' as

$$E_{np} = E - R_E E' - \omega_o \ , \tag{9}$$

where $\omega_o = 2.23$ MeV is the deuteron binding energy.

The inelastic cross section is written as

$$\frac{d\sigma}{d\Omega dE'} = \frac{\alpha^2}{4E^2} \sin^4\left(\frac{\theta}{2}\right) \left[W_2(\nu, Q^2)\cos^2\left(\frac{\theta}{2}\right) + 2W_1(\nu, Q^2)\sin^2\left(\frac{\theta}{2}\right)\right] \ , \tag{10}$$

where $W_1(\nu, Q^2)$ and $W_2(\nu, Q^2)$ are the inelastic structure functions. The inelastic data [2,14] from the present experiment provides new measurements of $W_1(\nu, Q^2)$, since all data were taken near 180°. Note that W_1 and W_2 may equivalently be written as functions of any pair of variables such as E_{np} and x_D, which depend only on Q^2 and ν.

III. OVERVIEW of the EXPERIMENT

The experimental apparatus has been discussed in detail elsewhere [15,16], so only a brief overview will be given here. The new threshold inelastic data were obtained during a 180° electron scattering experiment in which measurements were also made of quasielastic scattering [14,17], as well as elastic electron-deuteron [15,18] and electron-proton [15,17] scattering. The threshold inelastic data, which only used the 180° spectrometer, were taken simultaneously with the elastic *ed* measurements, in which deuterons recoiling near 0° were detected in coincidence with scattered electrons using a separate spectrometer.

Experimental conditions such as the spectrometer design could not be simultaneously optimized for the elastic, quasielastic, and threshold inelastic data taking. The elastic data were given priority in order to measure the magnetic form factor of the deuteron. Since elastic events were tagged by detecting recoil deuterons, high energy resolution for the electron spectrometer was not required. Inelastic events could not be tagged by detecting recoil protons in coincidence with scattered electrons since there was a large background of protons from other processes. Also, most of the protons fell outside the recoil spectrometer acceptance. Due to the small elastic cross section, long liquid deuterium targets and spectrometers having a large angular acceptance were needed. These properties compromised the resolution in E' to the extent that the corresponding resolution in E_{np} was as large as 20 MeV (see Eq.(9)) for the 20 cm liquid targets. Because of this, the data were analyzed using a resolution unfolding procedure in order to make comparisons with theoretical predictions, which are generally constrained to a small E_{np} range near threshold.

The experiment, identified as NE4, was carried out at the Stanford Linear Accelerator Center (SLAC) in two separate running periods. These occurred during the summer of 1985 (NE4-I) and spring of 1986 (NE4-II) respectively. Data were taken with electron beams of energy E = 0.734, 0.843, 0.885, 0.934, 1.020, 1.102, 1.201, and 1.279 GeV, produced by the Nuclear Physics Injector [19] with a maximum intensity of 5×10^{11} electrons per 1.6 μsec pulse at a repetition rate of 150 Hz. These beam energies correspond to Q^2 values at threshold of 1.21, 1.49, 1.61, 1.74, 1.99, 2.23, 2.53, and 2.76 (GeV)/c^2 respectively. Energy-defining slits limited the uncertainty in E to ±0.35%.

The electron beams were transported to a 180° spectrometer system [16] in End Station A. The entire spectrometer system is shown in Fig. 3. A series of three bending magnets $B_1 - B_3$ transported incident electrons toward the target. Dipole B_2 was symmetrically located between B_1 and B_3 and was remotely movable along a line perpendicular to the electron beam. This construction accommodated the different bending angles required for each beam energy. The incident beam then passed through the quadrupole triplet $Q_1 - Q_3$ into 10 or 20 cm long liquid deuterium cells.

The liquid deuterium and hydrogen target cells were machined out of an aluminum casting, and each 20 cm long cell included two aluminum endcaps of thickness 3.44×10^{-2} g/cm^2 through which the incident beam passed. Electrons scattered from the target endcaps represented the largest expected source of background, hence the endcaps were made as thin as possible while safely supporting two atmospheres of pressure from the liquid deuterium within. Two aluminum hymens, 6.86×10^{-3} g/cm^2 thick, isolated the target vacuum chamber and a wire array of average thickness 1.4×10^{-2} g/cm^2 was used to measure the beam position. The deuteron spectrum at $Q^2 = 1.21$ (GeV/c)^2 used a 10 cm target cell with 1.92×10^{-2} g/cm^{-2} thick endcaps, while all other threshold data were taken with the 20 cm cell.

Electrons scattered near 180° returned through $Q_1 - Q_3$ and were momentum-dispersed by spectrometer dipoles B_3 and B_4. Quadrupoles $Q_1 - Q_3$ provided the focussing strength needed to obtain a large solid angle for the electron spectrometer without unduly disturbing the incident beam. This solid angle $\Delta\Omega$, averaged over $\pm 0.5\%$ in relative momentum δ, was 22.4 msr for the 10 cm target, and 21.5 msr for the 20 cm target. Corrections for the non-uniformity in the electron spectrometer acceptance [15] were generally small since threshold inelastic data were analysed only in the range $-3.5\% \leq \delta \leq +3.5\%$, where the acceptance was fairly constant.

Electrons transmitted through the target passed through the quadrupole triplet $Q_4 - Q_6$ and were deflected by B_5 into a remotely movable, water-cooled beam dump. The focussing strengths of $Q_4 - Q_6$ were chosen to maximize transmission of deuterons into the recoil spectrometer for the elastic data while maintaining an acceptable beam spot size on the dump. The positively charged nuclei recoiling near 0° were deflected by B_5 toward the recoil spectrometer, which was used only in the elastic measurements. The dipole magnets $B_6 - B_8$ of this spectrometer separated recoil deuterons from a large background of lower momentum particles generated in the target.

For track reconstruction, the electron spectrometer contained six multi-wire proportional chambers (MWPC) spaced 20 cm apart. Two planes of plastic scintillation counters were used for triggering and fast timing. A large background of pions was rejected by a threshold gas Čerenkov counter and by measuring the energy deposited in a 40-segment array of lead-glass blocks.

The various voltage pulses from the detectors were carried by fast Heliax cables to CAMAC electronic modules in the counting house above End Station A. The quantities to be recorded for each scattering event were read from the CAMAC modules by a PDP-11 microcomputer and transferred to a VAX 11/780 computer for logging onto magnetic tape. The same VAX 11/780 computer was used both for analysing data on-line and for most of the subsequent off-line analysis.

IV. DATA ANALYSIS

The measured differential cross section per nucleon is given by

$$\frac{d^2\sigma(E,E')}{d\Omega dE'} = \left[\frac{1}{S_f D\epsilon(\Delta\Omega(\delta))}\right]\left[\frac{R_C(E,E')}{N_e\rho L N_A}\right]\frac{N(E,E')}{\Delta E}\ , \qquad (11)$$

where $N(E,E')$ is the number of counts in an energy bin of width ΔE centered on E', corrected for the expected number of counts from ed elastic scattering and for inelastic scattering from the hymens, wire array, and target endcaps. These corrections, as well as the radiative corrections factors $R_C(E, E')$, are discussed in more detail below. The factor S_f ranged from 0.9 to unity, and is a correction for multiple events within a beam pulse, since only the first event in each pulse was analysed. The electronic dead time correction factor D was always within 1% of unity while ϵ, the product of the detector efficiencies, ranged from 94 to 96%. The factor N_A is Avogadro's number, L is the target length, ρ is the target density, and N_e is the number of incident electrons.

A correction of $< 4\%$ was made for pions misidentified as electrons. Electrons were identified by the large pulse heights they produced in both the Čerenkov counter and the shower counter. Misidentification of pions as electrons could only occur when pions produced a large hadronic shower (for example, by charge exchange to π°), and at the same time either a random hit or a pion-produced knock-on electron ($\approx$ 1% probability) generated a large pulse height in the Čerenkov counter. No correction for electrons from the processes such as: $\gamma d \rightarrow \pi^\circ d$, $\pi^\circ \rightarrow \gamma\gamma$, $\gamma \rightarrow e^+e^-$ were made since estimates for this correction showed it to be $< 3\%$.

As is customary for threshold electron scattering, the cross sections per deuteron were expressed as a differential in E_{np}, using

$$\frac{d^2\sigma}{d\Omega dE_{np}} = \frac{1}{2}\frac{d^2\sigma}{d\Omega dE'}\frac{dE'}{dE_{np}}, \tag{12}$$

where the factor of two is to convert from cross sections per nucleon to cross section per deuteron.

A. Subtraction of Events Originating Outside the Target

The measured spectra include a background of electrons scattered from the hymens, wire array, and target endcaps. It was necessary to evaluate this background carefully since its contribution grows to 100% at large negative E_{np}, where scattering from the deuteron is kinematically forbidden. Also, the resolution unfolded results discussed below were sensitive to the presence of any residual signal in the electron spectra at large negative E_{np}.

The total background counting rates were measured in separate data runs using empty targets which were replicas of the full ones, except with endcaps thicker by a factor of 8.55 for the 20 cm and 8.20 for the 10 cm cells. The thicker endcaps on the empty target cells provided both a faster counting rate and approximately the same total radiation length as the full targets. This last condition made for similar radiative correction factors for the full and empty target endcaps.

Evaluation of the background contribution was complicated by the fact that the spectrometer solid angle for the aluminum hymens, wire array, and the two endcaps of the target were all substantially different. Also, if the scattering at 180° occurred in the downstream endcap or hymen, both the incident and scattered electrons must traverse the target. Thus, electrons interacting downstream of the target undergo energy losses for the full targets which are not present for the empty cells. These complications are discussed below.

The spectrometer solid angle $\Delta\Omega$ depends on the location z of the scattering vertex in addition to the relative momentum δ. A Monte-Carlo program [20] was used to generate distributions of events in δ with the scattering vertex held at fixed z positions. An example of such a distribution is shown in Fig. 4a, where the scattering vertex was held at the location of the upstream endcap. The distributions for other values of z are similar in shape, but vary considerably in overall magnitude, with the downstream hymen having the smallest solid angle. Each distribution was fit with a sixth order polynomial curve, and the ratios of the fits were used to evaluate the relative contribution of each background source. The ratio of distributions for the downstream to upstream endcaps is shown in Fig. 4b.

A further complication is the difference between the cross sections per nucleon for the copper wire array and aluminum target endcaps and hymens, due to the larger Fermi momentum for copper compared to aluminum. The ratio of these cross sections was obtained from a y-scaling analysis of existing data (see Fig. 4 of Ref. [21]) and yielded a correction factor of 1.1 for the wire array contribution.

The experimentally determined quantities were C_f and C_e, the total counts per unit incident electron for full and empty targets, given by

$$C_i(E,E') = \frac{1}{S_f \epsilon N_e D} N_R(E,E') \ , \tag{13}$$

where $N_R(E,E')$ is the raw number of counts corrected for spectrometer acceptance only. For example, C_f is given by

$$C_f = C_h + C_w + rC_E + C_D + rC'_E + C'_h \ , \tag{14}$$

where C_D is the desired contribution from liquid deuterium alone, C_h, C_w, and C_E are the contributions from the hymens, wire array, and target endcaps, and r is the ratio of full/empty target endcap thicknesses. The primes on C'_E and C'_h indicate that these quantities have been corrected for ionization losses in the full targets. To correct for these ionization losses, C'_E and C'_h were evaluated at $(E-\Delta E, E'+\Delta E)$ instead of (E,E'), where ΔE is the most probable energy loss

[22], approximately 5.8 MeV for 20 cm of liquid deuterium. Corresponding losses within the endcaps, hymens, and wire array were found to be negligible.

The total measured empty target contribution C_e is given by a similar expression. The ionization losses were neglected in this case as they were not significant. Since these data had poor statistics compared to the full target data, a smooth fit to the empty target data was used.

It was found best to fit the data using the quantity $E^2C_e(E,E')$, which is proportional to the inelastic structure function $W_1(Q^2,\nu)$. Fig. 5a shows this quantity for all incident energies E as a function of the scaling variable ω'. The data define a relatively smooth curve except for the spectrum at the highest ω', corresponding to $Q^2 = 1.21$ (GeV/c)^2. A three parameter fit to the empty target data was obtained using the form

$$\ln(E^2C_e(E,E')) = a_1 + a_2E + a_3E\omega' \ . \tag{15}$$

This fit yielded a χ^2 value of 1.06 per degree of freedom. The result, shown in Fig. 5b and c, was used in the endcap subtraction for all of the threshold inelastic data. The resulting errors in $C_e(E,E')$ ranged typically from 5% to 30%. Using the ratios of solid angles and thicknesses of each background source and the fits to the empty target data, the desired contribution from deuterium could be extracted.

In order to determine the sensitivity to the choice of fit to the empty target data, several fits with up to nine free parameters were obtained. The variation in the final cross sections due to the choice of fit is discussed in Sec. IV C, and was only significant for the $Q^2 = 1.21$ GeV/c^2 data.

The counts per unit charge before and after background subtraction are shown in Fig. 6 for the lowest and highest values of Q^2: 1.21 and 2.76 (GeV/c)^2. This correction is relatively small for momenta $\delta \leq -2\%$, where the deuterium cross section is large. However, the size of the correction is essentially 100% for $\delta \geq 1\%$, as expected. After subtracting the non-deuterium contributions, all spectra were consistent with zero for large negative E_{np}.

B. Radiative Corrections

Radiative corrections were performed to correct for bremsstrahlung and straggling of the incident and scattered electrons in the target medium. Bremsstrahlung occurs both as external radiation in the fields of nuclei distinct from the scattering nucleus, and as internal radiation at the scattering vertex. The radiative corrections were carried out using the equivalent radiator procedure of Mo and Tsai [23]. In this approach, the internal bremsstrahlung is modelled by two external radiators, placed before and after the scattering vertex. Since both E and E' depend on the radiated photon energy, the procedure involves integrations over a model for the unradiated cross section $\sigma(E, E')$. The "radiated" cross sections $\sigma_R(E, E')$ are obtained by convoluting $\sigma(E, E')$ with a normalized bremsstrahlung function. In order to perform the required integrations, it was necessary to interpolate the models of $\sigma(E, E')$ in both E and E'. For a given incident energy E, the theoretical models [4] used for $\sigma(E, E')$ were calculated at discrete values of E'. Cross sections at intermediate values of E' were obtained by linear interpolation. For the interpolation in incident energy E a simple power law fit was used. The E-dependence of a typical cross section model is shown for $E_{np} = 1$ and 12 MeV in Fig. 7. Since only the threshold region was investigated, the required range in E and E' was only a few percent.

The large range of material in the target before and after scattering caused substantial differences in the radiative correction factors as a function off target length. This was taken into account by calculating the corrections at each of 40 positions equally distributed along the target length. The most probable energy loss corresponding to the thickness of each layer was used to correct E and E'. Radiative correction factors $R_C(E,E') = \sigma(E,E')/\sigma_R(E,E')$ were calculated separately for each target section with $E_{np} > 0$. The correction factors increased approximately linearly with increasing depth into the target, as expected.

Shown in Fig. 8a,b are the separate contributions to the radiated cross section $\sigma_R(E,E')$ from Landau straggling and bremsstrahlung, for $(E,E') = (0.734, 0.3958)$ GeV, as a function of Δ, a convergence parameter [23] for the improper integrations over E and E'. In the present case, Δ is constrained to a few MeV, and the Landau contribution is small relative to the bremsstrahlung effect.

Unfortunately, as shown in Fig. 8c, the calculated radiative correction factors displayed a sizable dependence on Δ. This occurred because the straggling energy loss was comparable to the relative energy E_{np}, and the Mo-Tsai approximations break down under these conditions. Because the Landau terms were small, the radiative correction factors $R_C(E,E')$ were calculated using the bremsstrahlung terms only. This removed the lower constraint on Δ, which could then be made arbitrarily small, though still nonzero. The final correction factors $R_C(E,E')$, using bremsstrahlung only and averaged over target segments, had negligible dependence on Δ for any value below $\Delta = 1$ eV.

The radiative correction factors averaged over target segment are shown in Fig. 9 for $Q^2 = 1.21$ and 2.76 (GeV/c)^2. The values of $R_C(E,E')$ were calculated separately for each of two widely-divergent input models [4]. One model used $F_1(Q^2)$ coupling for the MEC and went smoothly to zero at the break-up threshold, while the other model had $G_E(Q^2)$ coupling and a strong enhancement at threshold. Since these two models represent the largest variation in the E_{np} dependence near threshold (other predictions [4,12] lie in between), the adopted set of radiative correction factors was the average of correction factors obtained from the two input models. Errors were assigned as half the difference between the two sets of correction factors and ranged typically from ±3% to ±8% of the average correction factor.

C. Resolution Unfolding

As previously noted, the data have relatively coarse energy resolution due to the intrinsic spectrometer resolution, ionization energy losses, multiple scattering, and the spread in incident beam energy. This total resolution ranged from ±5 to ±9 MeV in E_{np}. The attempt to unfold resolution effects from the data was motivated by the objective of determining the Q^2 dependence of the electrodisintegration cross section near threshold. Since the true cross section near the deuteron breakup threshold may vary rapidly with E_{np}, the resolution unfolding procedure is necessarily model-dependent.

Resolution effects have been treated using two different methods. In the first method, theoretical models were convoluted with Monte-Carlo determined [20] resolution functions and compared with the data. These results will be described below. In the second method, a model-dependent procedure was used to extract resolution unfolded cross sections, *i.e.*, cross sections free of resolution smearing effects, given by

$$\sigma_{exp}(E,\delta) = \int_{-\infty}^{\delta_T} R(\delta-\delta')\sigma(E,\delta')d\delta' \left[\int_{-\infty}^{+\infty} R(\delta')d\delta'\right]^{-1} , \qquad (16)$$

where $R(\delta')$ is the Monte-Carlo calculated resolution function, $\sigma_{exp}(E,\delta)$ represents the experimental data, and δ_T is the electron momentum at threshold relative to the deuteron elastic peak. Resolution functions were obtained by Monte-Carlo methods using the known electron spectrometer matrix elements. The spread in beam energy, and energy losses in the and targets and the wire chambers were all taken into account. The true cross section, $\sigma(E,\delta)$, was represented by a polynomial expansion,

$$\sigma(E,\delta) = \Sigma_{i=1}^{N} a_i \delta^{i'} \;\; E_{np} > 0 \; , \qquad (17)$$

$$\sigma(E,\delta) = 0 \;\; E_{np} < 0 \; ,$$

where N ranged from 2 to 4. These polynomials were inserted into Eq. (16), and the coefficients adjusted to give the best fit to the experimental data using a least-squares fitting routine. Such polynomial representations adequately describe available theoretical predictions for the shape of deuteron cross sections near threshold. Choices other than polynomials are feasible, but were not investigated.

The dominant systematic error arose from an uncertainty [16] of ±0.25% in the scattered electron energy E'. This yielded errors of ±10% to ±30% in the cross sections and contributed the largest variations in the resolution unfolded results. The size of these variations in the unfolded cross sections was evaluated by shifting the data by ±0.25% in δ and repeating the least-squares fit in each case. The reduced chi-squares for these fits ranged from 1.0 to 1.9 with an average of 1.3.

Typical fits to the radiatively corrected data for $Q^2 = 2.53$ (GeV/c)^2 are shown in Fig. 10. The three solid curves correspond to momentum shifts of ±0.25% and 0%.

Figs. 11, 12, and 13 show, for three values of Q^2, the cross sections $\sigma(E,\delta)$ from 2nd, 3rd, and 4th order polynomial fits to the radiatively corrected data. In each figure panel, the three curves correspond to the three momentum shifts δ of ±0.25% and 0% for a given choice of polynomial order. Although these cross sections fits are consistent with a non-zero cross section at the break-up threshold, the large dependence on the shifts in δ makes it impossible to draw any firm conclusions regarding the shape of the true cross section at threshold.

The resolution unfolded cross sections for all Q^2 were averaged over the relative kinetic energy E_{np} from 0 to a maximum E_{np}^M for comparison with averaged theoretical predictions as well as previous data. The E_{np}-averaged results for each value of Q^2 are shown as a function of E_{np}^M in Figs. 14 to 16. The curves in each figure panel correspond to the various choices of momentum offset and polynomial order. For a given E_{np}^M, the final unfolded result at each Q^2 was chosen as the centroid of the curves. Results from earlier experiments have usually been averaged over E_{np} from 0 to 3 MeV. As seen in Figs. 14 to 16, the large systematic spreads in the resolution unfolded results are dramatically reduced by averaging over a larger range of E_{np}, 0 to 10 MeV. The 0 to 10 MeV range was chosen since it is comparable to the experimental resolution. The present results ware compared to similarly averaged predictions in Section V.

The spectrum at $Q^2 = 1.21$ (GeV/c)^2 was analysed using both a three and nine-parameter fit to the corresponding empty target data, and the results are shown in Figs. 14a,b. The final cross sections in this case were obtained as the average of the two set of results.

The systematic errors in the unfolding procedure were estimated from the observed variation among the curves for each Q^2 in Figs. 14 to 16. For example, the E_{np}-averaged cross sections tend to fall into three groups corresponding to the momentum shifts applied to the data. This variation in the results was the largest systematic uncertainty, ranging from ±20% of the centroid for a 0 to 10 MeV range of E_{np} to ±70% for a 0 to 5 MeV range. Systematic errors due to the choice of polynomial order for the unfolded results were similarly estimated, and they varied from ±5% for a 0 to 10 MeV range to ±30% for a 0 to 5 MeV range. An additional error of $< \pm 10\%$ was due to the estimated uncertainty in the width of the Monte-Carlo resolution function. All of the systematic errors discussed above were added in quadrature to form the total error. Statistical errors in the resolution unfolded cross sections were negligible in comparison.

V. COMPARISON WITH THEORY

A. Predictions Folded With the Experimental Energy Resolution

One of the present experimental goals is to test for the influence of non-nucleonic effects such as MEC and, possibly, quark clusters in the deuteron wave-function. If, for example, MEC have a strong effect on the predictions up to $E_{np} = 20$ MeV, then the present resolution unfolded results constitute a legitimate test of E_{np}-averaged models.

Theoretical indications for the importance of MEC at large E_{np} are presented in Fig. 17, where several meson-nucleon predictions [4] and a hybrid quark-hadron prediction [12] are shown for the lowest and highest Q^2 values of the present experiment. The calculations including MEC are all considerably lower than the IA calculation, with the differences decreasing slowly with increasing E_{np}. At $E_{np} = 20$ MeV, the calculation [4] using F_1 coupling for the MEC is about 50% of the IA calculation at $Q^2 = 1.21$ (GeV/c)^2, and only 15% of the IA calculation at $Q^2 = 2.76$

(GeV/c)^2. Since any deviation from the IA is a measure of the influence of non-nucleonic effects, it is clear that for the models studied, MEC contribute strongly over a relatively large range of E_{np}.

Fig. 17 emphasizes the large differences that exist between calculations with different treatments of the MEC. For $E_{np} \leq 10$ MeV these variations can exceed an order-of-magnitude, and they remain large for E_{np} up to 20 MeV. Also evident in Fig. 17 are the substantial differences between the Yamauchi *et al.* [12] hybrid quark-hadron model calculations and the Arenhövel *et al.* [4] meson-nucleon calculations. Such variations between the theoretical predictions are preserved, even for a resolution in E_{np} as large as 10 MeV.

The coarse energy resolution of the present data motivated the use of two methods of comparison with theoretical predictions. The model-dependent resolution unfolding procedure has already been discussed, and the resulting comparisons with theory will be presented below. A less model-dependent procedure is to compare the actual data with predictions folded with Monte-Carlo determined resolution functions.

The convolution integral with respect to E_{np} can be written as

$$\sigma_s(E, E_{np}) = \int_0^{\infty} R(E_{np} - E'_{np})\sigma(E, E'_{np})dE'_{np} / \int_{-\infty}^{\infty} R(E'_{np})dE'_{np} \, , \qquad (18)$$

where $\sigma(E, E_{np})$ is the theoretical cross section, $R(E_{np})$ is the resolution function, and $\sigma_s(E, E_{np})$ is the resolution-smeared cross section.

Radiatively corrected data at six values of elastic four-momentum transfer squared Q^2 are shown in Figs. 18 and 19. The error bars represent total statistical and systematic uncertainties, added in quadrature. The ±0.25% uncertainty in scattered electron energy E' produced the largest systematic error in the cross sections.

Also shown in Figs. 18 and 19 are several non-relativistic predictions [4,12] smeared by the experimental resolution function according to Eq. (18). Within ≈ 3 MeV of threshold, electroproduction proceeds primarily through an M1 spin-flip transition to an unbound ${}^1S_0\ T = 1$ scattering state. However, for E_{np} greater than a few MeV, higher order partial waves contribute to the electrodisintegration cross section. The meson-nucleon predictions of Arenhövel *et al.* [4] take account of all electric and magnetic transitions with $L \leq 4$, where L is the orbital angular momentum of the final state. The hybrid quark-hadron calculations of Yamauchi *et al.* [12] take account of 12 different final np states and 28 transitions. Thus, the comparison of these predictions with the present data for E_{np} up to 20 MeV is justifiable.

The meson-nucleon predictions shown in Figs. 18 and 19 all use the Paris potential [7] to describe the deuteron wave function. Calculations with both the $G_E(Q^2)$ and $F_1(Q^2)$ electromagnetic form factors for the MEC are represented. The calculations employing $G_E(Q^2)$ use two different choices for the neutron form factor $G_{En}(Q^2)$: $G_{En}(Q^2) = 0$ and the model of Gari and Krümpelmann [24]. These choices have a sizeable effect on the calculations, although it should be noted that the first choice is strongly favored by recent data [9]. The models with Dirac coupling describe the data better up to $Q^2 \approx 2$ (GeV/c)^2, while those with Sachs coupling exhibit comparable agreement at higher Q^2 values.

The effects of six-quark clusters in the deuteron wave function are generally expected to be small. Exploratory quark-inspired models [10,11,12] are plagued by high sensitivity to poorly-constrained parameters. The hybrid quark-hadron model of Ref. 12 is in fair agreement with the higher Q^2 data shown in Fig. 19, but lies below the lower Q^2 data shown in Fig. 18.

To summarize this section, none of the non-relativistic predictions [4,12] is in quantitative agreement with the data over the entire Q^2-range of 1.2 to 2.7 $(\mathrm{GeV/c})^2$, although some calculations can describe the data in a more limited Q^2 range. In particular, understanding of the present data relies heavily on resolving the issue of what electromagnetic form factor is appropriate for the MEC. Fully relativistic meson-nucleon calculations and more rigorous quark-hadron models are needed.

B. Predictions Compared With Resolution Unfolded Data

In Section IV, a model-dependent procedure for extracting resolution unfolded cross sections was described. The results for each Q^2 were averaged over various ranges of E_{np}. A range of 0 to 10 MeV in E_{np} was chosen to be compatible with the present energy resolution, and much larger than the ±0.25% uncertainty in E'. Also, the model dependence was found to be substantially reduced for larger averaging ranges.

Averaging over a range of 0 to 10 MeV requires some justification since previous experiments [1] at lower Q^2 have better resolution than the present high Q^2 experiment, and the published results were averaged over $E_{np} = 0$ to 3 MeV. For comparison, Fig. 20 shows three different theoretical predictions [4,12] averaged both over the range of E_{np} from 0 to 3 and over the range from 0 to 10 MeV. For the model of Yamauchi *et al.* [12] and the G_E calculation of Arenhövel *et al.* [4], the 0 to 3 MeV averaging range to gives somewhat larger results than the 0 to 10 MeV range. This is expected since these models predict an enhancement in the cross section close to threshold. However, the differences are small, on the same order as the experimental errors, and the differences between the models is much larger than differences due to the averaging range. The F_1 calculation of Arenhövel *et al.* [4] shows a larger difference between the two averaging ranges, especially at low Q^2. In this case the 0 to 10 MeV results are higher than the 0 to 3 MeV results, because this model predicts no enhancement at threshold. Nevertheless, the differences due to the choice of MEC coupling (F_1 versus G_E) are much larger than the differences due to the averaging range.

In short, at least up to $E_{np} = 20$ MeV, differences between various predictions are much larger than effects from different E_{np}-averaging ranges and errors introduced by the resolution unfolding procedures. We therefore feel it is reasonable to compare the present experimental results, averaged over 0 to 10 MeV, with similarly averaged theoretical predictions.

Resolution unfolded results from the present experiment averaged over 0 to 10 MeV are compared with similarly averaged predictions [4,12] shown on the right hand side of Fig. 21. The error bars include both statistical and systematic uncertainties, and primarily reflect the uncertainty in E'. Higher resolution data from a recent experiment [25] performed at the Bates Linear Accelerator Center up to $Q^2 = 1.6$ (GeV/c)^2 are in reasonable agreement with the present data. On the left hand side of Fig. 21 finer resolution data from previous experiments [1,25] are compared with the theoretical predictions of Ref. 12 at $E_{np} = 1.5$ MeV, and of Ref. [4], averaged over the range 0 to 3 MeV. The differences due to averaging over 0 to 3 *versus* 0 to 10 MeV, are indicated by the small discontinuities in the curves at $Q^2 = 1.1$ (GeV/c)^2. Despite the relatively coarse resolution in E_{np} and systematic errors from resolution unfolding, the present data can discriminate between the available models. The data indicate a change in slope with increasing Q^2 around

1 (GeV/c)^2, which is qualitatively consistent with "diffraction features" observed in all of the models.

Although several models predict the change of slope shown in Fig. 21 at roughly the correct Q^2 value, they are not in accord with the data over the entire Q^2 range. While the inclusion of MEC certainly improves the agreement for $Q^2 < 1$ (GeV/c)^2, severe discrepancies remain at higher Q^2. Comparisons of the present data with other predictions are given elsewhere [25,26,27]. The dependence on nucleon-nucleon potential, nucleon form factor parametrization, treatment of MEC and isobars, and possible quark clusters are examined in these references. All of these inputs are found to have a substantial influence on non-relativistic predictions. One of the calculations in [27] agrees fairly well with all of the available data.

C. Ratio of Inelastic Structure Functions

As shown in Eq. (10), the cross section for inelastic electron scattering can be written in terms of two inelastic structure functions, $W_1(E_{np}, Q^2)$ and $W_2(E_{np}, Q^2)$. The present backward angle measurements of threshold inelastic and quasielastic [14] scattering yield $W_1(E_{np}, Q^2)$, while the results of a previous measurement [28] at forward angles, are to a good approximation proportional to $W_2(E_{np}, Q^2)$. In the IA the ratio W_1/W_2 is approximately equal to unity, independent of E_{np} and Q^2. This ratio is also insensitive to the choice of wave function and nucleon form factors. Any measured deviations of this ratio from unity indicate the influence of interaction effects beyond the nucleons-only IA framework.

The previous data [28] used to obtain $W_2(E_{np}, Q^2)$ were taken at a scattering angle of 8°. The cross sections are shown in Fig. 22 for eight values of Q^2

in the range 0.2 to 1.0 (GeV/c)^2. These data have been resolution unfolded using the model-dependent procedure described above, and the error bars are total statistical and systematic uncertainties. As in the present experiment, the largest systematic errors in the resolution unfolding procedure were caused by an uncertainty of ±0.05% in E'. A smaller systematic error [28] of 7.5%, not associated with the resolution unfolding, has been added in quadrature. To obtain the ratios W_1/W_2, it was necessary to extract $W_2(E_{np}, Q^2)$ at the same E_{np} and Q^2 values of the $W_1(E_{np}, Q^2)$ results. The data of Fig. 22 were interpolated to the desired kinematic values using a two-dimensional fit in the incident energy E and the Bjorken scaling variable x_D. The fit function had the form

$$f(E, x_D) = e^{h(E,x_D)} , \tag{19}$$

where

$$h(E, x_D) = a_1 + a_2 x_D + a_3 E + a_4 E x_D^2 + a_5 E^2 + a_6 E^2 x_D , \tag{20}$$

and is represented by the curves in Fig. 22. Each curve corresponds to a different value of the beam energy E, ranging from 7 to 14 GeV.

The ratios W_1/W_2, extracted at three average values of Q^2, are shown in Fig. 23. In each case, W_1/W_2 is approximately unity for $E_{np} > 50$ MeV, but decreases as $E_{np} \to 0$, in agreement with earlier results by Titov [29] at lower Q^2. Thus, the quasi-free mechanism is dominant above $E_{np} \approx 50$ MeV, whereas near the break-up threshold, interaction effects are important over the entire range of Q^2 studied.

The curves in Fig. 23 represent calculations [4,30] that use wave functions derived from the Paris potential and take into account final state interactions, MEC, and Δ resonances. All of the predictions of Ref. [4] yield $W_1/W_2 \approx 1$ for $E_{np} > 40$ MeV, in agreement with the data. Below $E_{np} = 50$ MeV, the IA calculation and a calculation that includes MEC with Sachs coupling produce essentially constant values of W_1/W_2 over the entire range of E_{np}, in marked disagreement with the data. The prediction that uses Dirac coupling for the MEC decreases rapidly as $E_{np} \to 0$, in qualitative agreement with the data. This is due to the absence of any enhancement near the deuteron break-up threshold (see Fig. 17). The prediction of Ref. 30 does not extend into the threshold region and lies somewhat below the results of Ref. [4] at large E_{np}.

All predictions shown in Fig. 23 are in agreement with the experimentally determined W_1/W_2 ratios above $E_{np} \approx 50$ MeV. This suggests that non-nucleonic effects are relatively unimportant compared with the IA interaction in this region. In contrast, for E_{np} below 40 MeV, the models depend critically on the choice of coupling for the MEC and are in poor agreement with the data. This reemphasizes the earlier conclusion that non-relativistic predictions for the region near the deuteron break-up threshold are generally inadequate at the Q^2 values of the present experiment.

VI. CONCLUSIONS

Inelastic cross sections measured at $E_{np} < 40$ MeV show clear evidence for scattering mechanisms beyond the IA. However, no non-relativistic prediction is in quantitative agreement with the data now that the measurements have been extended to $Q^2 = 2.7$ (GeV/c)^2.

Despite coarse energy resolution, the present data are sensitive to MEC, which are predicted to have strong effects up to $E_{np} = 20$ MeV. Thus, the comparisons with predictions given here and elsewhere [25,26,27] are justified.

The present resolution unfolded results, when compared with earlier data [1] at lower Q^2, have provided the first evidence of a change of slope in the cross section near $Q^2 \approx 1$ (GeV/c)^2. This change of slope is consistent with more recent experimental results [25] at higher energy resolution. It is clear that the present experimental results have opened many new questions in a region where the deuteron wave function, non-nucleonic degrees of freedom, and relativistic effects are all important.

ACKNOWLEDGEMENTS

We would like to acknowledge the support of J. Davis, R. Eisele, C. Hudspeth, J. Mark, J. Nicol, R. Miller, L. Otts, and the rest of the SLAC staff. We also thank H. Arenhövel, J.-M. Laget, and Y. Yamauchi for providing numerical results of their calculations.

Table I. Cross sections per deuteron nucleus for inelastic electron-deuteron scattering near break-up threshold. The beam energy E and relative energy E_{np} are evaluated at the center of the target. The errors include statistical and systematic contributions added in quadrature.

E =0.734 GeV		E =0.843 GeV		E =0.885 GeV		E =0.934 GeV	
E_{np} (MeV)	$d\sigma/d\Omega dE_{np}$ (fb/sr-MeV)	E_{np} (MeV)	$d\sigma/d\Omega dE_{np}$ (fb/sr-MeV)	E_{np} (MeV)	$d\sigma/d\Omega dE_{np}$ (fb/sr-MeV)	E_{np} (MeV)	$d\sigma/d\Omega dE_{np}$ (fb/sr-MeV)
-22.4	0.12 ± 0.29	-25.4	0.01 ± 0.06	-26.6	-0.02 ± 0.03	-27.9	-0.02 ± 0.03
-20.6	0.03 ± 0.29	-23.3	0.01 ± 0.06	-24.4	-0.01 ± 0.04	-25.6	0.00 ± 0.03
-18.7	-0.49 ± 0.25	-21.2	-0.01 ± 0.06	-22.2	-0.07 ± 0.04	-23.3	-0.01 ± 0.03
-16.9	-0.81 ± 0.31	-19.1	-0.05 ± 0.06	-20.0	-0.03 ± 0.04	-20.9	0.01 ± 0.03
-15.1	0.16 ± 0.35	-17.0	0.03 ± 0.07	-17.7	0.03 ± 0.04	-18.6	0.00 ± 0.03
-13.2	-0.32 ± 0.34	-14.9	0.05 ± 0.08	-15.5	-0.04 ± 0.04	-16.2	0.01 ± 0.03
-11.4	-0.18 ± 0.41	-12.8	-0.05 ± 0.07	-13.3	-0.05 ± 0.04	-13.9	0.01 ± 0.03
-9.6	0.27 ± 0.49	-10.7	0.01 ± 0.08	-11.1	-0.08 ± 0.06	-11.6	0.02 ± 0.04
-7.7	0.54 ± 0.59	-8.6	0.00 ± 0.10	-8.9	0.07 ± 0.09	-9.2	0.04 ± 0.04
-5.9	0.52 ± 0.56	-6.4	0.04 ± 0.13	-6.7	0.09 ± 0.10	-6.9	0.09 ± 0.05
-4.1	0.84 ± 0.59	-4.3	0.14 ± 0.14	-4.4	0.32 ± 0.12	-4.6	0.12 ± 0.07
-2.2	2.30 ± 0.64	-2.2	0.52 ± 0.17	-2.2	0.29 ± 0.12	-2.2	0.21 ± 0.08
-0.4	0.53 ± 0.56	-0.1	0.57 ± 0.18	0.0	0.55 ± 0.14	0.1	0.33 ± 0.08
1.4	2.14 ± 0.73	2.0	0.62 ± 0.19	2.2	0.77 ± 0.14	2.4	0.42 ± 0.07
3.3	3.43 ± 0.87	4.1	1.00 ± 0.19	4.4	0.93 ± 0.15	4.8	0.43 ± 0.07
5.1	3.14 ± 1.04	6.2	1.50 ± 0.21	6.6	0.97 ± 0.17	7.1	0.56 ± 0.08
6.9	4.86 ± 1.11	8.3	1.24 ± 0.20	8.8	1.02 ± 0.19	9.4	0.64 ± 0.10
8.8	5.71 ± 1.18	10.4	1.45 ± 0.26	11.1	1.44 ± 0.24	11.8	0.72 ± 0.12
10.6	7.99 ± 1.29	12.5	1.69 ± 0.31	13.3	1.74 ± 0.26	14.1	0.79 ± 0.12
12.4	7.44 ± 1.27	14.6	1.88 ± 0.37	15.5	1.85 ± 0.27	16.5	1.04 ± 0.13
14.3	9.61 ± 1.45	16.7	3.12 ± 0.40	17.7	2.25 ± 0.29	18.8	1.15 ± 0.14
16.1	9.98 ± 1.55	18.9	2.77 ± 0.35	19.9	2.53 ± 0.31	21.1	1.01 ± 0.14
17.9	12.10 ± 1.76	21.0	3.21 ± 0.37	22.1	2.68 ± 0.32	23.5	1.41 ± 0.17
19.8	13.80 ± 1.83	23.1	2.95 ± 0.33	24.3	2.97 ± 0.33	25.8	1.47 ± 0.18
21.6	16.02 ± 1.89	25.2	3.58 ± 0.36	26.6	3.53 ± 0.35	28.1	1.82 ± 0.20
23.5	16.99 ± 1.91	27.3	4.44 ± 0.40	28.8	3.67 ± 0.35	30.5	1.84 ± 0.20

continued

Table I. continued.

E =1.020 GeV		E =1.102 GeV		E =1.201 GeV		E =1.279 GeV	
E_{np} (MeV)	$d\sigma/d\Omega dE_{np}$ (fb/sr-MeV)	E_{np} (MeV	$d\sigma/d\Omega dE_{np}$ (fb/sr-MeV)	E_{np} (MeV)	$d\sigma/d\Omega dE_{np}$ (fb/sr-MeV)	E_{np} (MeV	$d\sigma/d\Omega dE_{np}$ (fb/sr-MeV)
-30.3	0.038 ± 0.012	-32.6	0.001 ± 0.007	-35.3	0.000 ± 0.004	-37.4	-0.002 ± 0.002
-27.7	0.001 ± 0.013	-29.8	0.003 ± 0.008	-32.3	-0.004 ± 0.004	-34.2	-0.005 ± 0.002
-25.2	0.006 ± 0.013	-27.0	0.007 ± 0.010	-29.3	0.007 ± 0.006	-31.0	0.000 ± 0.003
-22.6	-0.006 ± 0.013	-24.3	-0.001 ± 0.009	-26.3	-0.002 ± 0.006	-27.8	-0.003 ± 0.002
-20.1	0.014 ± 0.018	-21.5	0.009 ± 0.009	-23.3	0.013 ± 0.007	-24.6	0.000 ± 0.003
-17.5	0.004 ± 0.016	-18.8	0.026 ± 0.011	-20.3	0.002 ± 0.005	-21.4	0.002 ± 0.004
-15.0	-0.009 ± 0.016	-16.0	-0.002 ± 0.008	-17.3	-0.002 ± 0.005	-18.2	0.003 ± 0.004
-12.4	0.027 ± 0.019	-13.3	0.016 ± 0.012	-14.3	0.016 ± 0.008	-15.0	0.005 ± 0.005
-9.9	0.023 ± 0.021	-10.5	0.019 ± 0.014	-11.2	0.006 ± 0.008	-11.8	0.010 ± 0.005
-7.3	0.055 ± 0.024	-7.7	0.034 ± 0.017	-8.2	0.010 ± 0.009	-8.6	0.004 ± 0.006
-4.8	0.069 ± 0.026	-5.0	0.049 ± 0.019	-5.2	0.036 ± 0.010	-5.4	0.025 ± 0.007
-2.2	0.083 ± 0.032	-2.2	0.068 ± 0.021	-2.2	0.053 ± 0.012	-2.2	0.028 ± 0.008
0.3	0.160 ± 0.040	0.5	0.098 ± 0.024	0.8	0.042 ± 0.011	1.0	0.047 ± 0.009
2.9	0.207 ± 0.041	3.3	0.157 ± 0.026	3.8	0.063 ± 0.013	4.2	0.042 ± 0.008
5.4	0.275 ± 0.047	6.0	0.145 ± 0.026	6.8	0.081 ± 0.014	7.4	0.067 ± 0.010
8.0	0.358 ± 0.054	8.8	0.183 ± 0.029	9.8	0.083 ± 0.016	10.6	0.041 ± 0.009
10.5	0.263 ± 0.054	11.6	0.199 ± 0.031	12.8	0.109 ± 0.018	13.8	0.069 ± 0.011
13.1	0.410 ± 0.065	14.3	0.262 ± 0.038	15.8	0.100 ± 0.017	17.0	0.078 ± 0.011
15.6	0.438 ± 0.067	17.1	0.263 ± 0.038	18.8	0.139 ± 0.020	20.2	0.071 ± 0.011
18.2	0.492 ± 0.066	19.8	0.259 ± 0.038	21.8	0.150 ± 0.020	23.4	0.062 ± 0.011
20.7	0.608 ± 0.074	22.6	0.334 ± 0.041	24.8	0.129 ± 0.022	26.5	0.091 ± 0.014
23.3	0.679 ± 0.074	25.4	0.365 ± 0.047	27.8	0.162 ± 0.024	29.8	0.100 ± 0.015
25.8	0.639 ± 0.074	28.1	0.352 ± 0.051	30.8	0.208 ± 0.027	33.0	0.103 ± 0.015
28.4	0.735 ± 0.076	30.9	0.422 ± 0.050	33.8	0.234 ± 0.028	36.2	0.144 ± 0.017
30.9	0.756 ± 0.076	33.6	0.502 ± 0.056	36.8	0.209 ± 0.027	39.3	0.134 ± 0.016
33.5	0.870 ± 0.077	36.4	0.556 ± 0.059	39.8	0.246 ± 0.029	42.5	0.114 ± 0.015

Table II. Ratio of the inelastic structure functions W_1/W_2 for inelastic electron-deuteron scattering. The relative energy E_{np} in units of MeV is evaluated at the target center, and the errors include both statistical and systematic contributions.

$< Q^2 >$=1.36 (GeV/c)^2		$< Q^2 >$=1.84 (GeV/c)^2		$< Q^2 >$=2.33 (GeV/c)^2	
E_{np}	W_1/W_2	E_{np}	W_1/W_2	E_{np}	W_1/W_2
9.4	0.178 ± 0.024	11.8	0.237 ± 0.035	14.3	0.386 ± 0.071
13.6	0.211 ± 0.027	16.9	0.317 ± 0.047	20.3	0.534 ± 0.094
17.8	0.320 ± 0.060	22.0	0.435 ± 0.068	26.3	0.525 ± 0.103
22.0	0.310 ± 0.061	27.1	0.441 ± 0.071	32.3	0.774 ± 0.147
26.2	0.368 ± 0.075	32.2	0.489 ± 0.077	38.3	0.730 ± 0.132
32.4	0.409 ± 0.065	38.5	0.428 ± 0.082	49.9	0.525 ± 0.129
40.3	0.521 ± 0.071	48.1	0.795 ± 0.113	61.4	0.734 ± 0.145
48.2	0.746 ± 0.089	57.6	0.541 ± 0.080	72.8	0.847 ± 0.147
56.1	0.812 ± 0.092	67.2	0.923 ± 0.115	85.6	0.711 ± 0.118
64.0	0.645 ± 0.073	76.8	0.743 ± 0.093	96.4	0.702 ± 0.106
71.9	0.796 ± 0.085	86.4	0.820 ± 0.097	107.1	0.857 ± 0.117
80.8	0.876 ± 0.114	96.0	0.827 ± 0.108	117.9	1.010 ± 0.130
88.3	0.931 ± 0.109	105.0	0.927 ± 0.108	128.7	0.764 ± 0.098
95.7	0.811 ± 0.095	114.0	0.931 ± 0.105	139.5	1.000 ± 0.120
103.1	0.892 ± 0.101	123.0	0.843 ± 0.094	151.5	0.877 ± 0.150
110.5	0.825 ± 0.094	132.0	0.856 ± 0.093	161.6	0.974 ± 0.140
118.0	0.924 ± 0.102	141.0	0.849 ± 0.090	171.7	1.050 ± 0.150
126.3	0.979 ± 0.122	151.3	1.010 ± 0.130	181.9	0.947 ± 0.130
		159.8	1.110 ± 0.130	192.0	1.040 ± 0.130

REFERENCES

[a] Present address: Saddleback College, Mission Viejo, CA 92691

[b] Present address: University of Pennsylvania, Philadelphia, PA 19104

[c] Permanent address: Georgetown University, Washington, D.C. 20057

[d] Present address: Stanford Linear Accelerator Center, Stanford, CA 94309

[e] Permanent address: School of Physics, Shizuoka University, Shizuoka, 422 Japan.

1. R. E. Rand *et al.*, Phys. Rev. Lett. **18**, 469 (1967); G. G. Simon F. Borkowski, C. Schmitt, V. H. Walther, H. Arenhövel, W. Fabian, Nucl. Phys. **A324**, 277 (1979); M. Bernheim *et al.*, Phys. Rev. Lett. **46**, 402 (1981); S. Auffret *et al.*, Phys. Rev. Lett. **55**, 1362 (1985).
2. R. G. Arnold *et al.*, Phys. Rev. C **42**, R1 (1990).
3. J. Hockert *et al.*, Nucl. Phys. **A217** 14 (1973); J. A. Lock, and L. L. Foldy, Ann. Phys. **93**, 276 (1975); W. Fabian, and H. Arenhövel, Nucl. Phys. **A258**, 461 (1976).
4. H. Arenhövel, Prog. Theo. Phys. Suppl. **91**, 1 (1987); S. K. Singh, W. Leidemann, H. Arenhövel, Z. Phys. **A331**, 509 (1988); A. Buchmann, W. Leidemann, H. Arenhövel, Nucl. Phys. **A443**, 726 (1985); H. Arenhövel, Nucl. Phys. **A374**, 532c (1982); H. Arenhövel, private communication.
5. J. Adam, Jr., and E. Truhlik, Czech. J. Phys. **B34**, 1157 (1984), and Few Body System Suppl., **1**, 261 (1986); J. Delorme, Nucl. Phys. **A446**, 65c (1985); E. Hadjimichael, Phys. Lett. **B172**, 156 (1986); J. M. Lina, and B. Goulard, Phys. Rev. **C34**, 714 (1986).
6. F. Gross and D. O. Riska, Phys. Rev. **C36**, 1928 (1987).

7. M. Lacombe, B. Loiseau, J.-M. Richard, R. Vinh Mau, J. Cote, P. Pires, R. De Tourneil, Phys. Rev. **C21**, 861 (1980).

8. R. Machleidt, K. Holinde, C. Eister, Phys. Rep. **149**, 1 (1987).

9. A. Lung, *et al.*, SLAC-PUB-5861, 1992, submitted to Phys. Rev. Lett.

10. L. S. Kisslinger, Phys. Lett **112B**, 307 (1982); Tan-Sheng Cheng and L. S. Kisslinger, Nucl. Phys. **A457**, 602 (1986).

11. L. Ya. Glozman, N. A. Burkova, E. I. Kochina, V. I. Kukulin, Phys. Lett. **B200**, 406 (1988).

12. Y. Yamauchi and M. Wakamatsu, Nucl. Phys. **A457**, 621 (1986); Y. Yamauchi *et al.*, Nucl. Phys. **A443**, 628 (1985); Y. Yamauchi, A. Buchmann, and A. Faessler, Nucl. Phys. **A 526**, 495 (1991); Y. Yamauchi, private communication.

13. E. D. Bloom and F. J. Gilman, Phys. Rev. **D4**, 2901 (1971).

14. R. G. Arnold *et al.*, Phys. Rev. Lett. **61**, 806 (1988).

15. P. E. Bosted, *et al.*, Phys. Rev. **C42**, 38 (1990).

16. A. T. Katramatou, G. Petratos, R. G. Arnold, P. E. Bosted, E. L. Eisele, R. Gearhart, Nucl. Instrum. Meth. **A267**, 448 (1988).

17. G. G. Petratos, Ph.D thesis, The American University, Washington, D.C., 1988.

18. R. G. Arnold *et al.*, Phys. Rev. Lett. **58**, 1723 (1987); A. T. Katramatou, Ph.D thesis, The American University, Washington, D.C., 1988.

19. R. F. Koontz, Roger Miller, G. Leger, R. Nelson, Particle Accelerator Conference, Proceedings, p. 3036, Vancouver, Canada, 1985.

20. A. T. Katramatou, SLAC Report No. SLAC-NPAS-TN-86-8, 1986.

21. D. B. Day *et al.*, Phys. Rev. Lett. **59**, 427 (1987).

22. L. D. Landau, J. Phys. USSR **8**, 201 (1944); R. M. Sternheimer and R. F. Peirls, Phys. Rev. **B3**, 3681 (1971).

23. Y. S. Tsai, SLAC Report No. SLAC–PUB–848, 1971; L. M. Mo and Y. S. Tsai, Rev. Mod. Phys. **41**, 205 (1969).

24. M. Gari and W. Krümpelmann, Z. Phys. **A322**, 689 (1985); Phys. Lett. **B173**, 10 (1986).

25. K. S. Lee *et al.*, Phys. Rev. Lett. **67**, 2634 (1991).

26. W. Leidemann, K.-M. Schmitt, and H. Arenhövel, Phys. Rev. **C42**, R826 (1990).

27. E. Truhlik and K.-M. Schmitt, Few-Body Systems **11**, 155 (1992).

28. W. P. Schütz *et al.*, Phys. Rev. Lett. **38**, 259 (1977), and R. G. Arnold, private communication for revised results.

29. Yu. I. Titov, Kharkov preprint, KhFTI-87-38 and Int. Symp. on Lepton and Photon Interactions at High Energy, Hamburg, FRG (1987); A. S. Esaulov, A. P. Rekalo, M. P Rekalo, Yu. I Titov, A. V. Akhmerov, E. M. Smelov, Yad. Fiz. **45**, 410 (1987).

30. J. -M. Laget, Phys. Lett. **199B**, 493 (1987); J. -M. Laget, Can. J. Phys. **62**, 1046 (1984), and private communication.

FIGURE CAPTIONS

1. An incident electron exchanges a virtual photon: (a) in the plane wave impulse approximation (PWIA) with no final state interactions; (b) in the distorted wave impulse approximation (DWIA), in which the nucleons interact after the photon exchange.
2. Three contributions to MEC in electron scattering: (a) single pion MEC; (b) pair production; (c) Δ resonance production.
3. The 180° spectrometer system of this experiment. The system is located between the SLAC 8 GeV/c and 20 GeV/c spectrometers. The elements B_1 to B_8 are dipole magnets, and Q_1 to Q_6 are quadrupoles. Also shown are the detectors, target chamber, beam dump, and the concrete and iron shielding.
4. (a) A Monte-Carlo generated distribution of events for incident electron energy $E = 0.889$ GeV. The scattering vertex is fixed at the location of the upstream full-target endcap and the error bars are statistical only. Similar distributions were generated with the scattering vertex at other locations, such as the downstream full-target endcap. Each 0.40% bin in relative momentum δ received 160 trials, which were ray-traced through the system using the electron spectrometer matrix elements [16,17]. The solid curve is a sixth order polynomial fit. (b) Ratio of distribution with the scattering vertex at the downstream endcap over the distribution at the upstream endcap (shown in (a)). The error bars were calculated using an error matrix for the polynomial fits.
5. (a) Empty target data for $Q^2 = 1.21, 1.49, 1.61, 1.74, 1.99, 2.23, 2.53$, and 2.76 $(\mathrm{GeV/c})^2$, shown as counts per unit incident electron charge multiplied by the square of the beam energy E as a function of the ω' scaling variable. (b) Empty target data as in (a) for $Q^2 = 1.21, 1.49, 1.74, 2.23$, and 2.76

$(\mathrm{GeV/c})^2$. The curves are a two-dimensional fit using E and ω' with three free parameters. (c) Data and curves as in (a) and (b), but for $Q^2 = 1.61, 1.99$, and 2.53 $(\mathrm{GeV/c})^2$.

6. Threshold inelastic data are shown for two values of Q^2. The data have not been radiatively corrected. The upper set of points without error bars have not been corrected for scattering in material outside the liquid deuterium target. The lower set of points have been corrected for these interactions. The errors bars include both statistical and systematic contributions.

7. Predicted electrodisintegration cross sections [4] as a function of incident energy E for two values of the relative neutron-proton kinetic energy E_{np}. The predictions use the Dirac electromagnetic form factor $F_1(Q^2)$ for the meson exchange currents (MEC) with electric neutron form factor $G_{En}(Q^2)$ of Ref. [24].

8. (a) The radiated cross section $\sigma_R(E, E')$ for $(E, E') = (0.735, 0.396)$ GeV as a function of convergence parameter Δ, for scattering from the upstream end of the target. Both total (solid curve) and individual contributions due to bremsstrahlung (dashed curve) and Landau straggling (dotted curve) are shown. (b) Same as (a) except for scattering near the downstream end of the target. (c) The resulting radiative correction factors $R_C(E, E')$ are shown for scattering from the front (solid curve), middle (dashed curve), and back (dotted curve) of the target.

9. Radiative correction factors, averaged over target length, are shown as a function of E_{np} for two values of Q^2. The values of E_{np} correspond to scattering from the center of the target. The results using two different theoretical representations of the true unradiated cross section [4] are shown.

10. Threshold inelastic data at $Q^2 = 2.53$ (GeV/c)^2 are shown as a function of relative momentum δ. The error bars include all systematic and statistical errors except for the systematic error due to the uncertainty in E'. The three solid curves are fits to the data using polynomial representations of the resolution unfolded cross section, as discussed in the text. Each curve corresponds to a choice of ±0.25%, or 0% momentum shift in the data.
11. Threshold inelastic data as in Fig. 10 are shown at three values of Q^2. The three curves in each panel represent phenomenological cross section models using a 2nd order polynomial with three choices of momentum shift, as in Fig. 10. These models were convoluted with the experimental resolution before being fit to the data. A three-parameter fit to the empty target data has been used, as described in the text.
12. Same as Fig. 11, except for 3rd order polynomial representation.
13. Same as Figs. 11 and 12, except for 4th order polynomial representation.
14. Resolution unfolded cross sections averaged over E_{np} from 0 to E_{np}^M are shown as a function of E_{np}^M. The dotted, dashed, and solid curves refer to a momentum shift of +0.25, −0.25 and 0% respectively. Each individual curve corresponds to a particular choice of polynomial order, 2nd to 4th. In (a) and (c), a three-parameter fit to the empty target data is used while in (b), results with a nine-parameter fit are shown.
15. Same as Fig. 14 except for $Q^2 = 1.61, 1.74$, and 1.99 (GeV/c)^2, and all results were obtained with a three-parameter fit to the empty target data.
16. Same as Fig. 15 except at $Q^2 = 2.23, 2.53$, and 2.76 (GeV/c)^2.
17. Various predictions as a function of E_{np} assuming perfect experimental resolution in E_{np}. The solid curves represent the hybrid quark-hadron model of Yamauchi *et al.*[12]. The other curves represent the meson-nucleon predic-

tions of Arenhövel *et al.*[4]. The dashed curves represent calculations with Dirac (F_1) coupling for the MEC. The dotted and dotdashed curves represent calculations with Sachs (G_E) coupling and $G_{En}(Q^2) = 0$ and $G_{En}(Q^2)$ of Ref. [24] respectively. The dashed-double-dotted curves represent the IA calculation.

18. Radiatively corrected data are shown at three values of Q^2. The error bars include contributions from both statistical and systematic errors. The curves are the meaning as in Fig. 17, but have been convoluted with the experimental resolution,. and the IA calculation is not shown.
19. Same as in Fig. 18 except at higher Q^2.
20. Two theoretical predictions of Arenhövel *et al.*[4] with F_1 and G_E coupling for the MEC, and the calculation of Yamauchi *et al.*[12] are shown as a function of Q^2 averaged over E_{np} from 0 to 3 and 0 to 10 MeV (indicated as '3' and '10' in the figure, respectively).
21. Threshold inelastic cross sections at 180° are shown as a function of Q^2. The meson-nucleon predictions of Arenhövel *et al.*[4] using the Paris potential are shown in the IA and with MEC using both Dirac and Sachs coupling as indicated. The hybrid quark-hadron model of Yamauchi *et al.*[12] is represented as the solid curve. All predictions and present data above $Q^2 = 1.1$ (GeV/c)^2 are averaged over E_{np} from 0 to 10 MeV. Below $Q^2 = 1.1$ (GeV/c)^2, previous data (open circles, Auffret *et al.* in Ref. [1] and all predictions are averaged over $E_{np} = 0$ to 3 MeV. The open squares represent recent data from Ref. [25], also averaged over $E_{np} = 0$ to 3 MeV.
22. Resolution unfolded electrodisintegration data from Ref. [28] are shown for $E = 6.519, 7.302, 8.981, 9.718, 10.407, 11.671, 12,821,$ and 14.878 in order from top to bottom. The data were taken at 8°, and the error bars are to-

tal statistical and systematic errors. The curves represent a six-parameter global fit.

23. Values of the ratio W_1/W_2 as a function of E_{np}, extracted for three values of average Q^2 from the present 180° data and forward angle data of Ref. [28]. The inner error bars are statistical errors only, and outer error bars include systematic uncertainties. The meson-nucleon predictions of Arenövel *et al.*[4] using the Paris potential are shown in the IA and with MEC using both Dirac (F_1) and Sachs (G_E) couplings. The meson-nucleon predictions of Laget [30] also use the Paris potential.

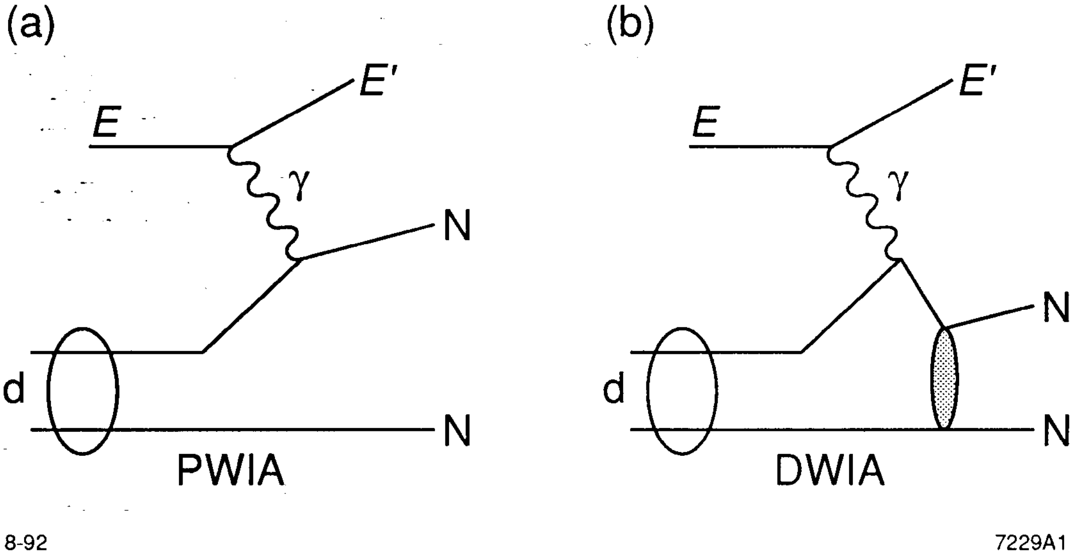

Fig. 1

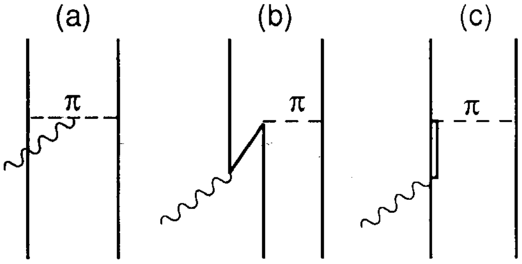

8-92 7229A2

Fig. 2

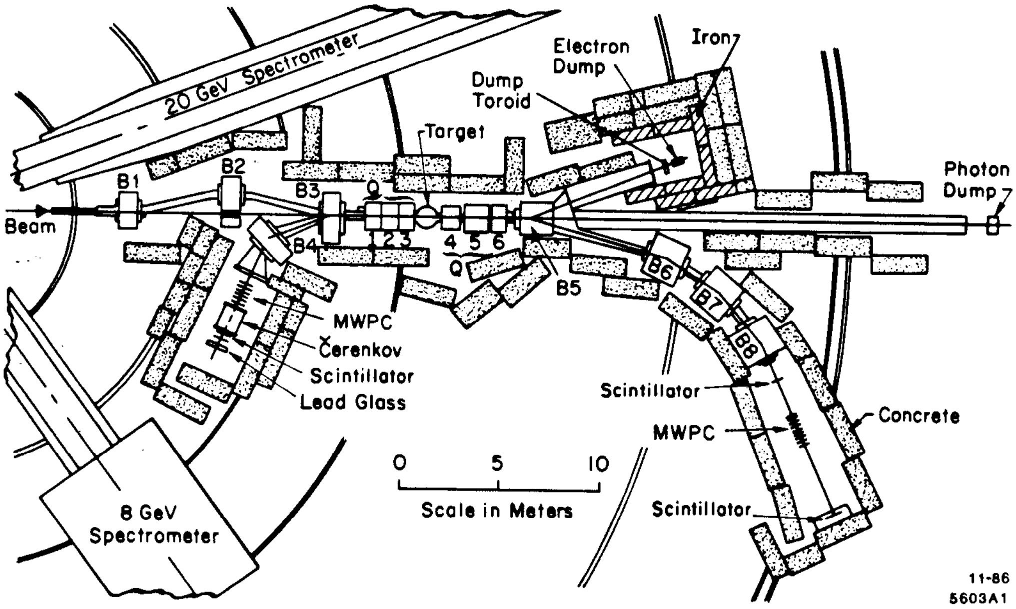
20 GeV Spectrometer
Electron Dump
Iron
Dump Toroid
Target
Photon Dump
B1
B2
B3
Q
1 2 3
4 5 6
Q
B4
B5
B6
B7
B8
Beam
MWPC
Čerenkov
Scintillator
Lead Glass
Scintillator
MWPC
Scintillator
Concrete
0
5
10
Scale in Meters
8 GeV Spectrometer
11-86
5603A1

Fig. 3

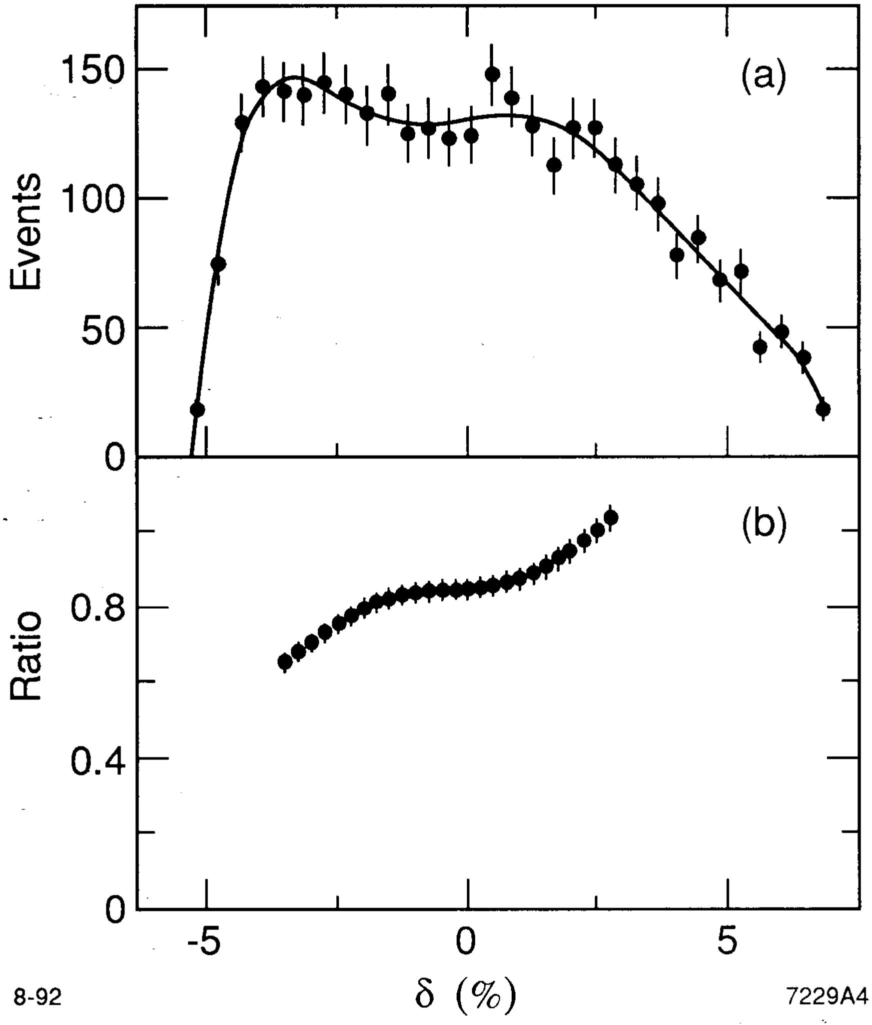

Fig. 4

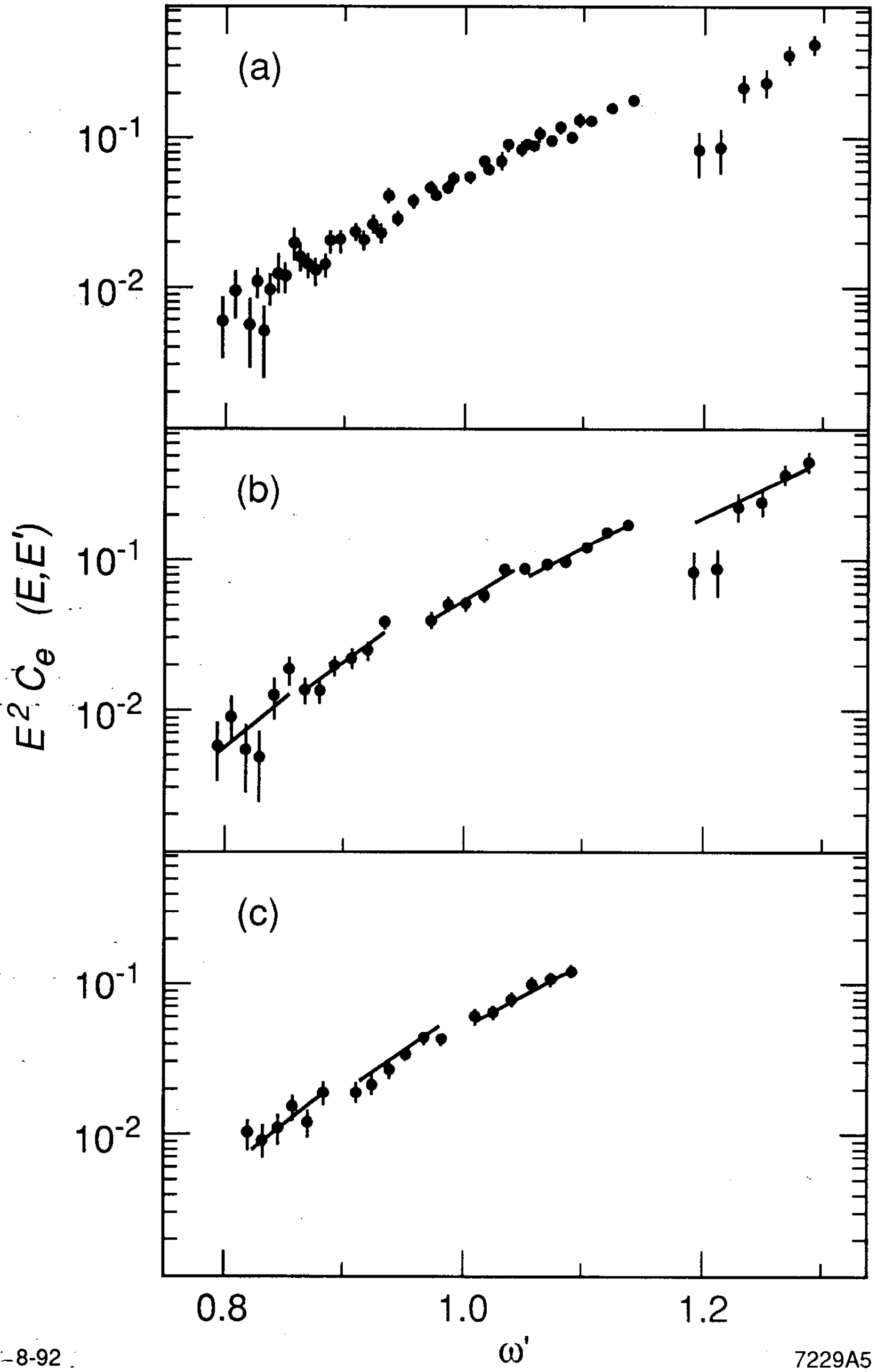

Fig. 5

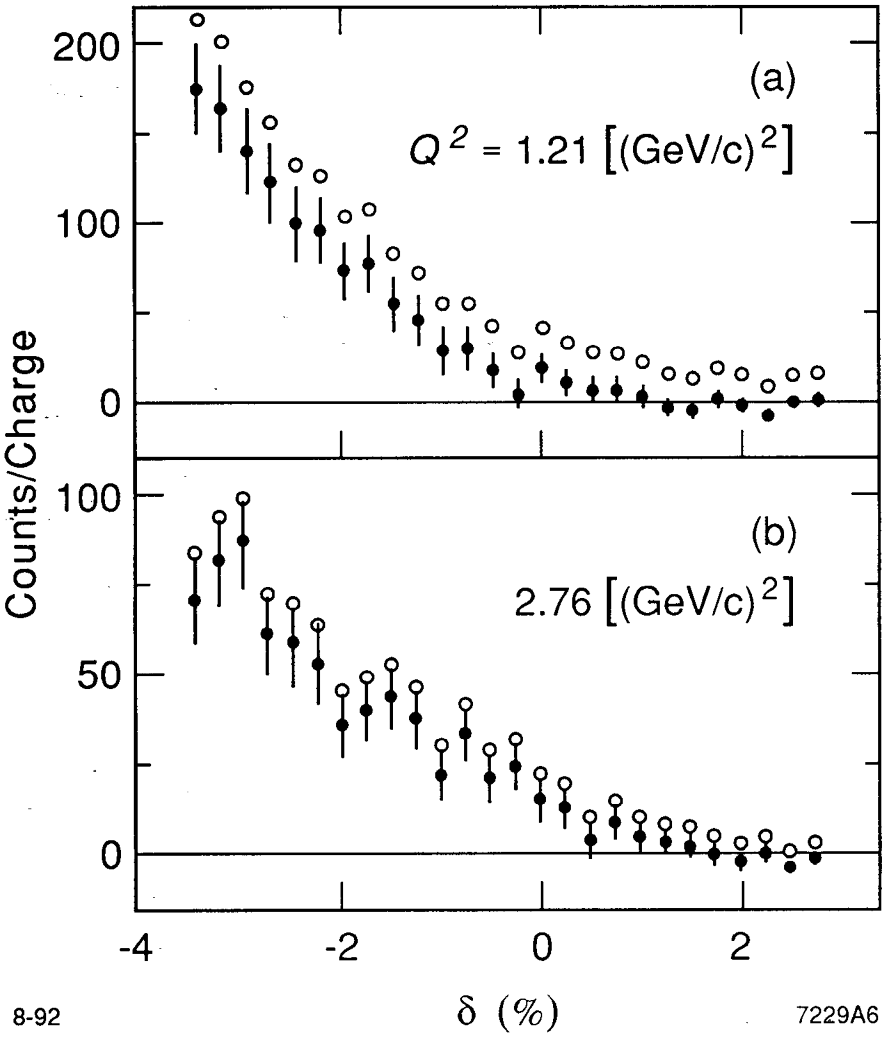
200
100
0
100
50
0
-4
-2
0
2
Counts/Charge
(a)
Q^2 = 1.21 [(GeV/c)^2]
(b)
2.76 [(GeV/c)^2]
δ (%)
8-92
7229A6

Fig. 6

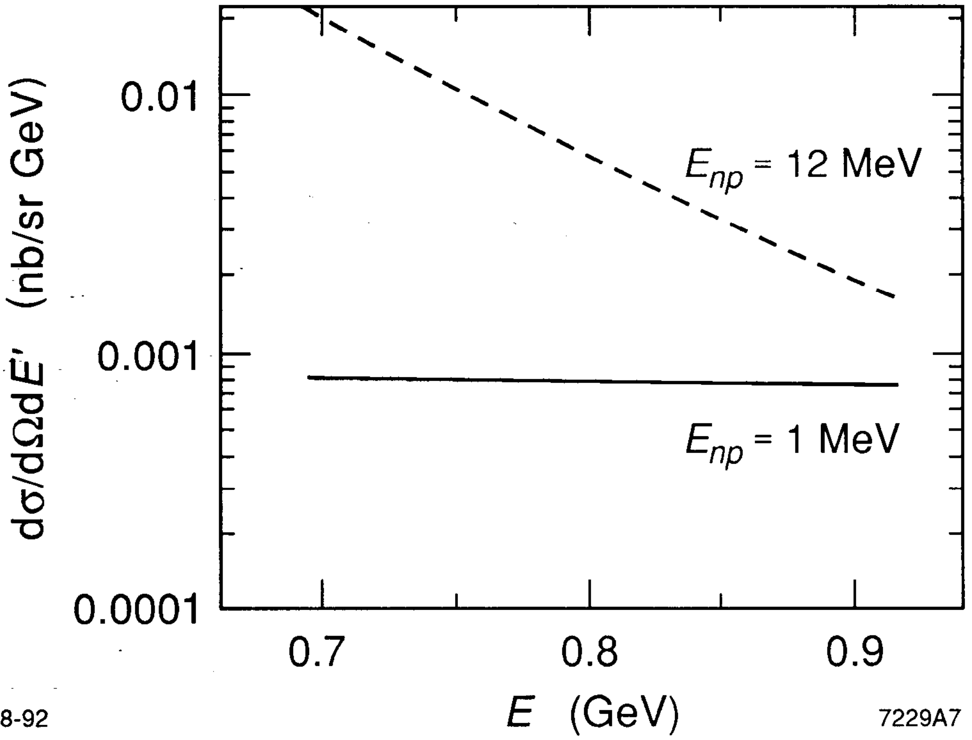

0.01
0.001
0.0001
dσ/dΩdE′ (nb/sr GeV)
E_{np} = 12 MeV
E_{np} = 1 MeV
0.7
0.8
0.9
E (GeV)
8-92
7229A7

Fig. 7

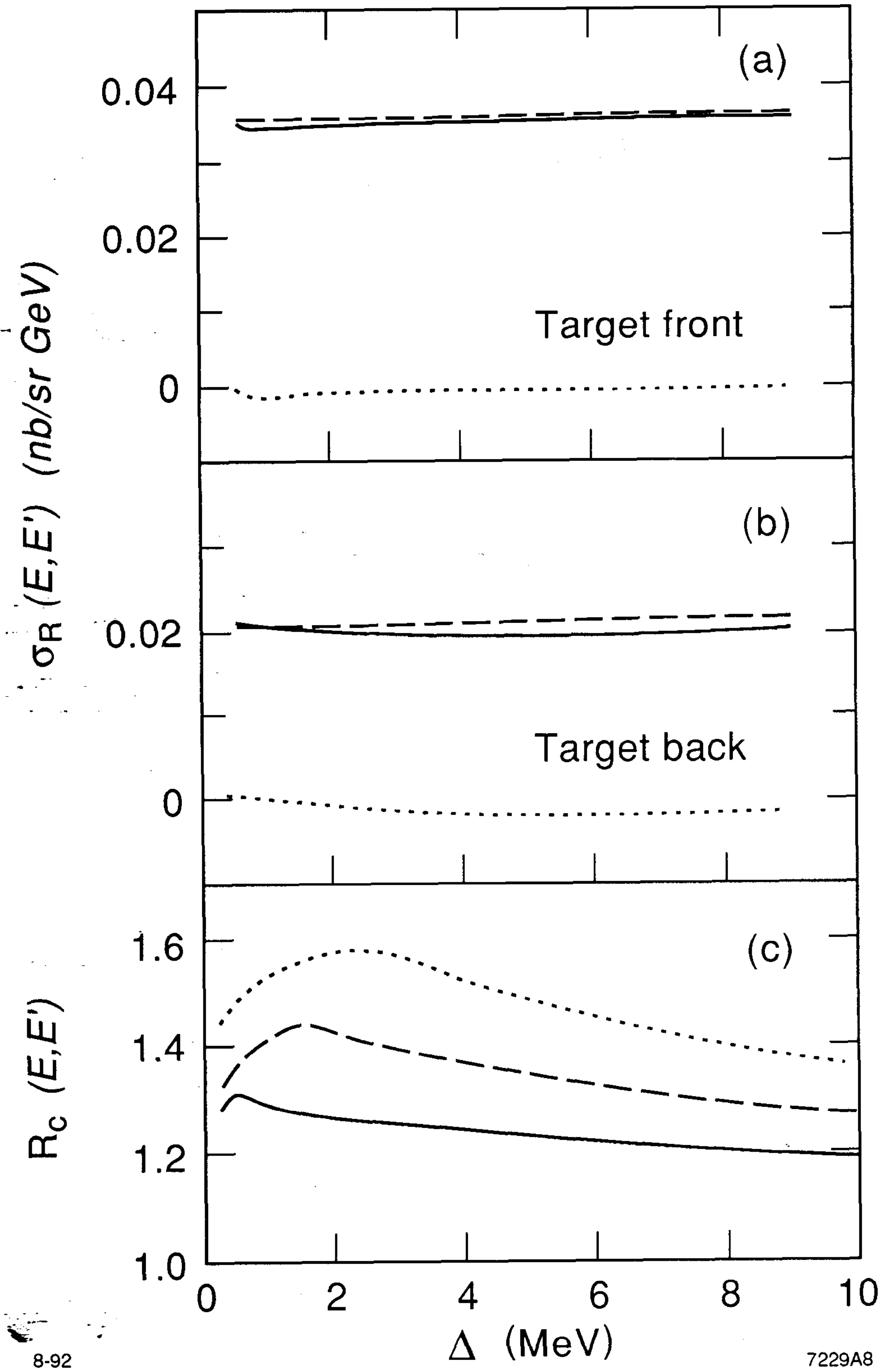
(a)
0.04
0.02
0
Target front
σR (E,E') (nb/sr GeV)
(b)
0.02
0
Target back
(c)
1.6
1.4
1.2
1.0
Rc (E,E')
0
2
4
6
8
10
Δ (MeV)
8-92
7229A8

Fig. 8

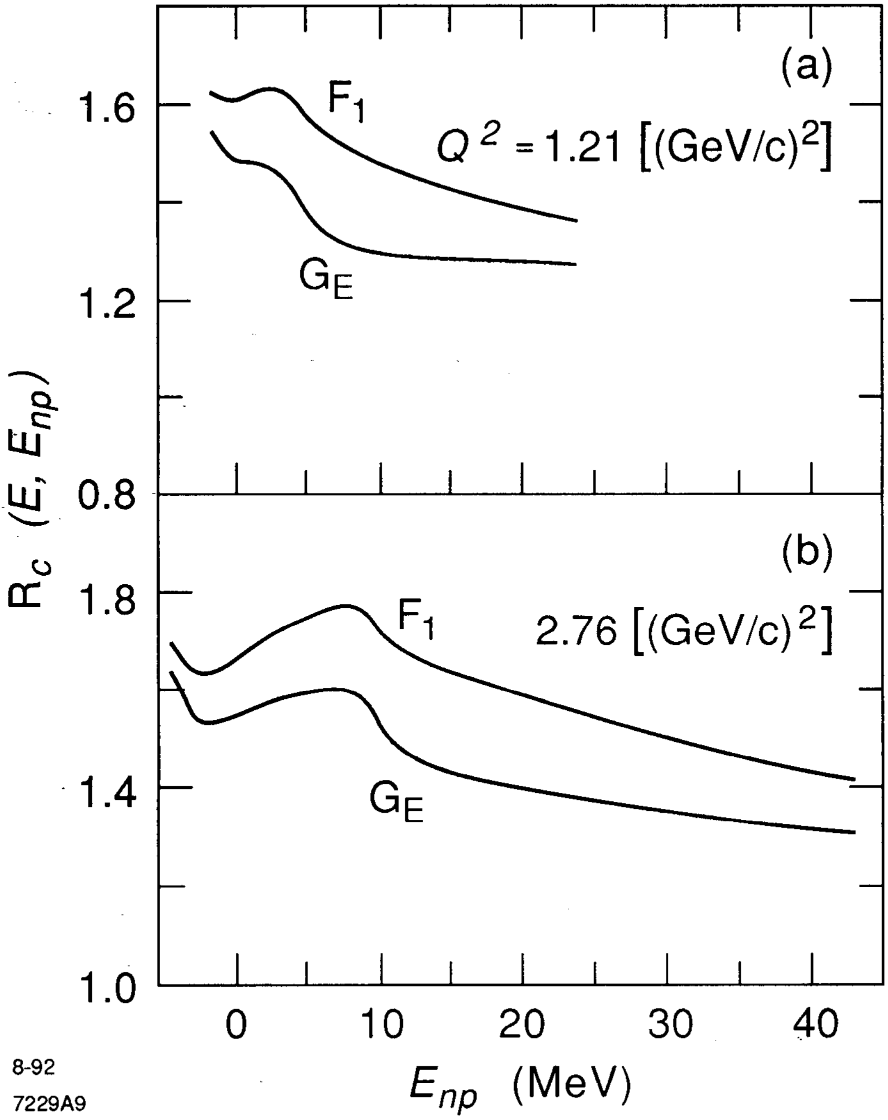
(a)
F1
GE
Q 2 = 1.21 [(GeV/c)2]
1.6
1.2
0.8
(b)
F1
GE
2.76 [(GeV/c)2]
1.8
1.4
1.0
Rc (E, Enp)
0
10
20
30
40
Enp (MeV)
8-92
7229A9

Fig. 9

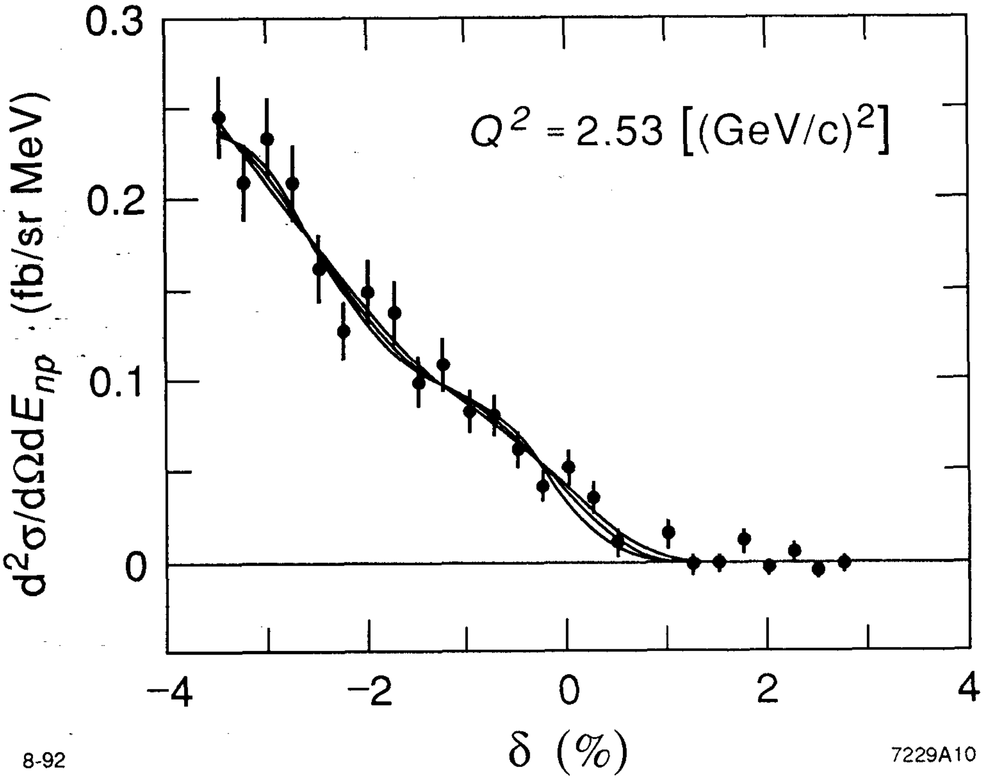
0.3
0.2
0.1
0
−4
−2
0
2
4
$Q^2 = 2.53 \ [(\mathrm{GeV/c})^2]$
$d^2\sigma/d\Omega dE_{np}$ (fb/sr MeV)
δ (%)
8-92
7229A10

Fig. 10

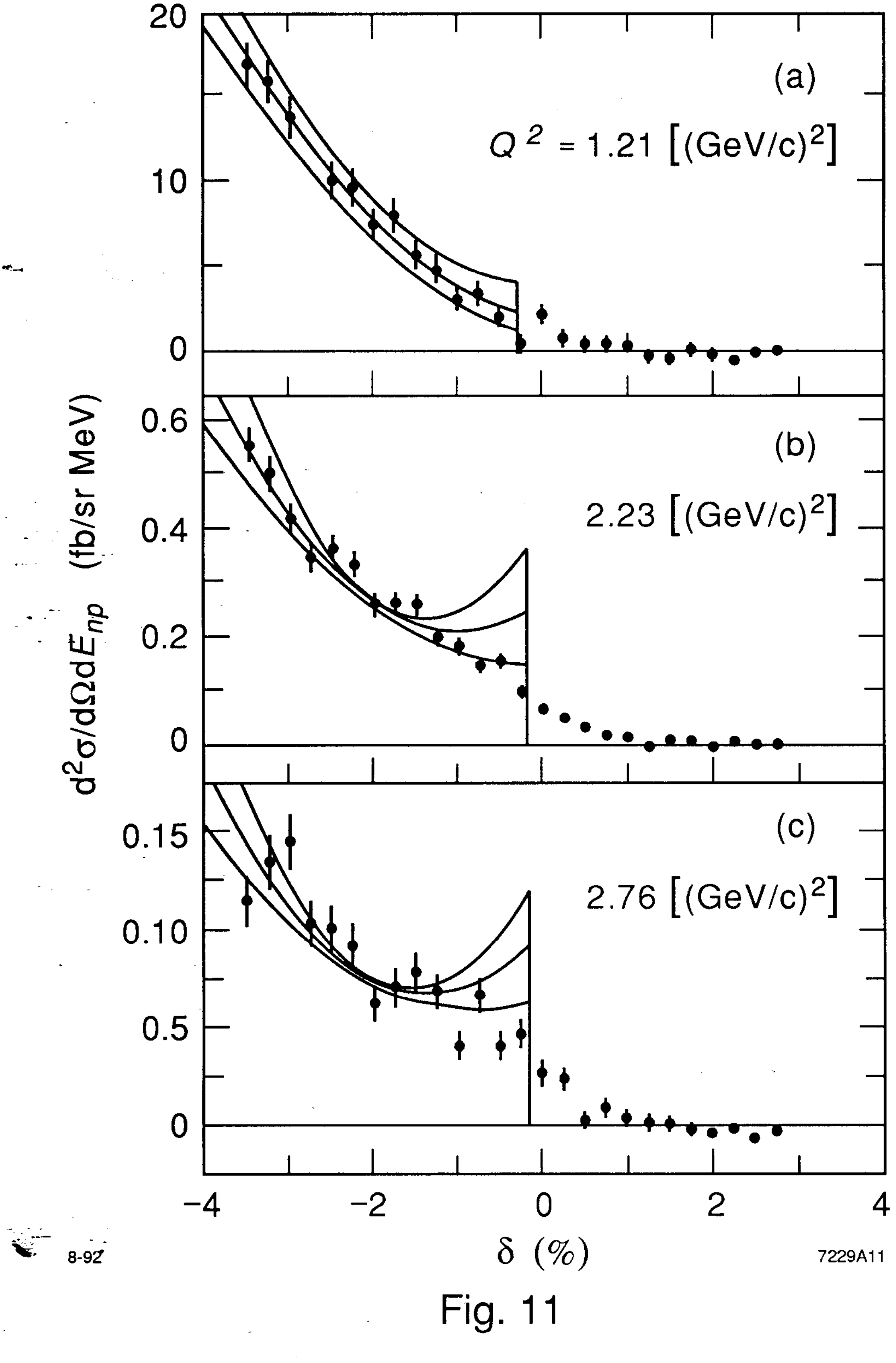

20
10
0
(a)
Q^2 = 1.21 [(GeV/c)^2]
0.6
0.4
0.2
0
(b)
2.23 [(GeV/c)^2]
0.15
0.10
0.5
0
(c)
2.76 [(GeV/c)^2]
$d^2\sigma/d\Omega dE_{np}$ (fb/sr MeV)
−4
−2
0
2
4
δ (%)
8-92
7229A11

Fig. 11

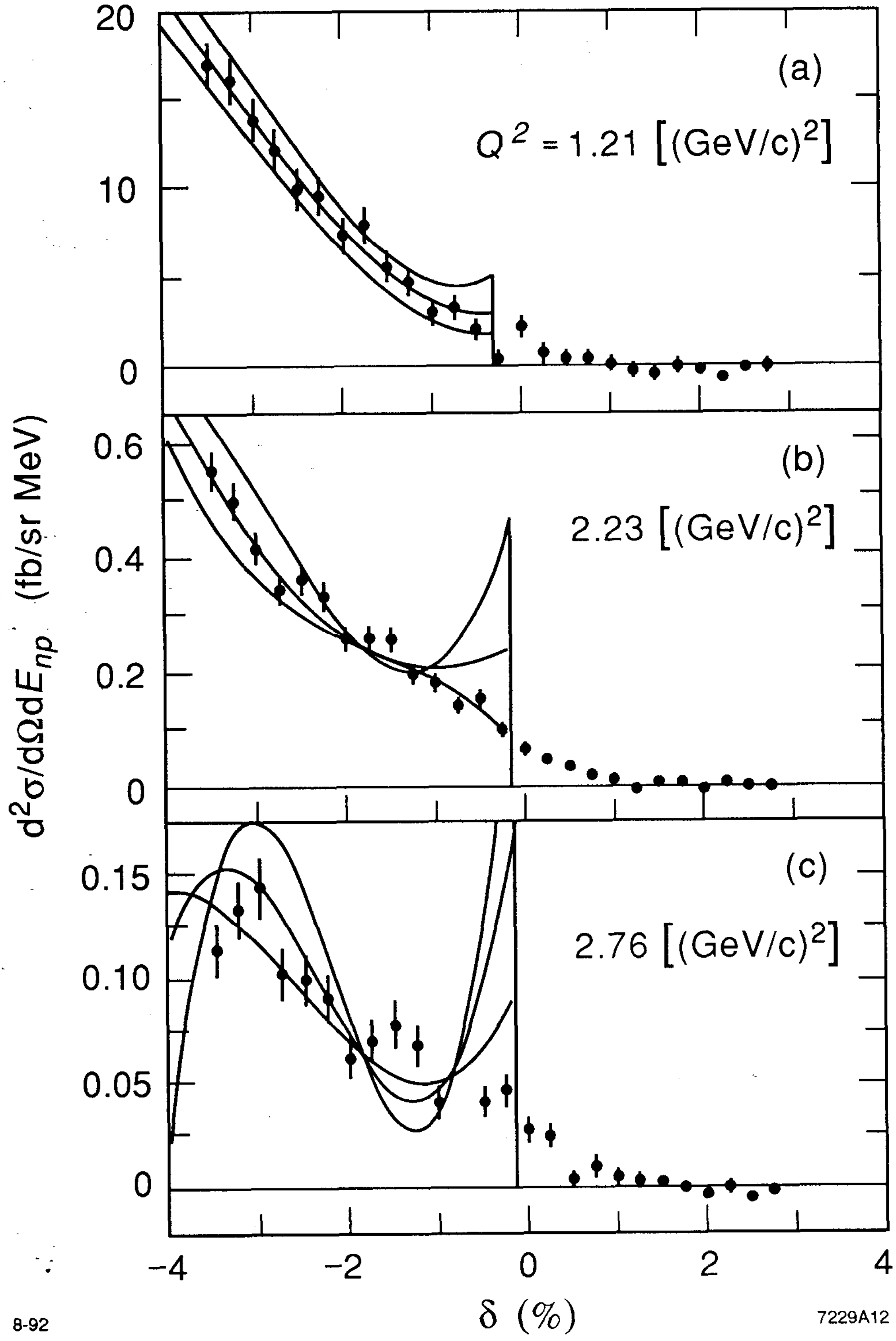
20
10
0
(a)
$Q^2 = 1.21$ [(GeV/c)^2]
0.6
0.4
0.2
0
(b)
2.23 [(GeV/c)^2]
0.15
0.10
0.05
0
(c)
2.76 [(GeV/c)^2]
$d^2\sigma/d\Omega dE_{np}$ (fb/sr MeV)
−4
−2
0
2
4
δ (%)
8-92
7229A12

Fig. 12

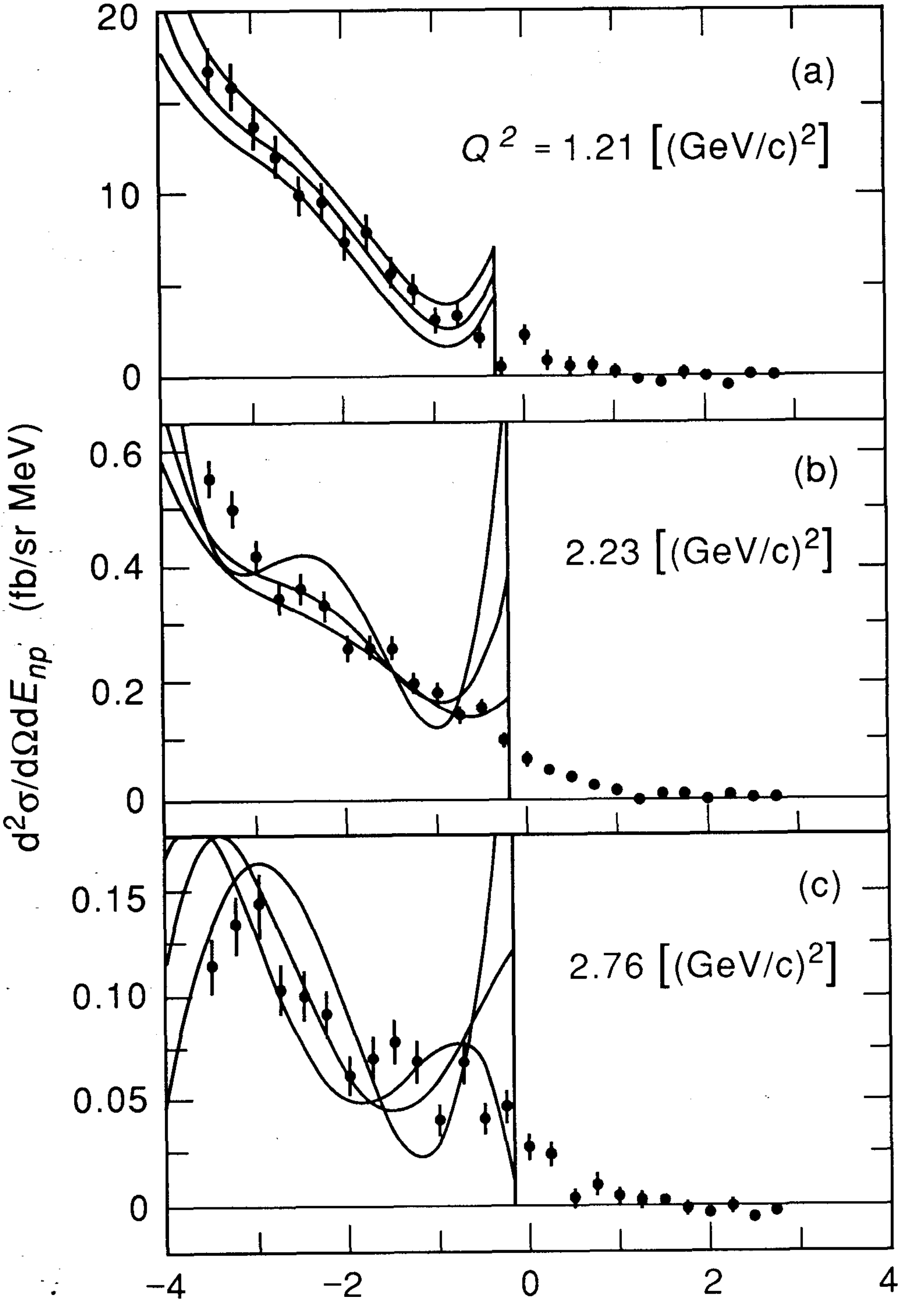

(a)
$Q^2 = 1.21\ [(\mathrm{GeV}/c)^2]$
(b)
$2.23\ [(\mathrm{GeV}/c)^2]$
(c)
$2.76\ [(\mathrm{GeV}/c)^2]$
20
10
0
0.6
0.4
0.2
0
0.15
0.10
0.05
0
$d^2\sigma/d\Omega dE_{np}$ (fb/sr MeV)
−4
−2
0
2
4
δ (%)
8-92
7229A13

Fig. 13

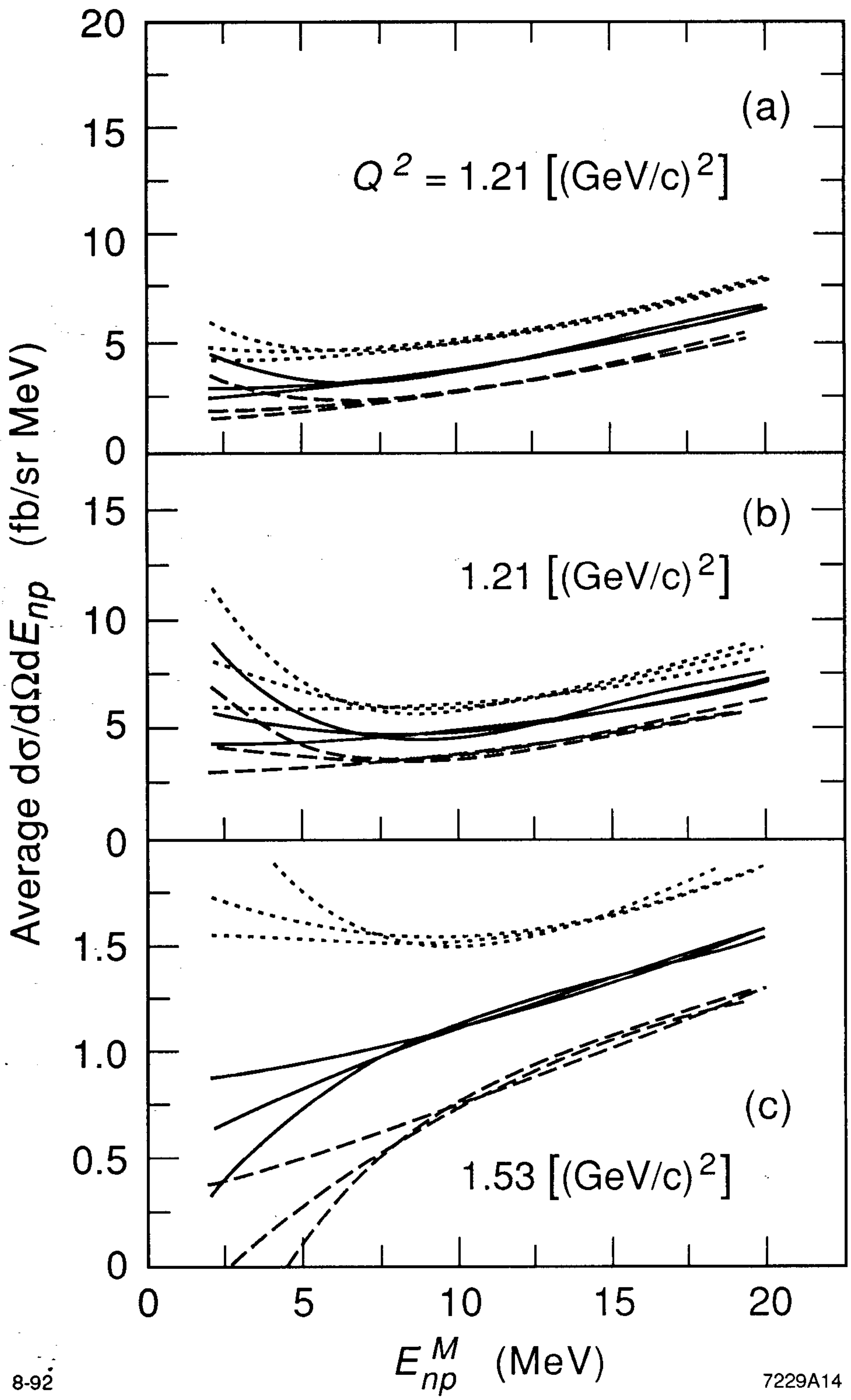
20
15
10
5
0
(a)
$Q^2 = 1.21$ [(GeV/c)^2]
15
10
5
0
(b)
1.21 [(GeV/c)^2]
Average dσ/dΩdE_{np} (fb/sr MeV)
1.5
1.0
0.5
0
(c)
1.53 [(GeV/c)^2]
0
5
10
15
20
E_{np}^M (MeV)
8-92
7229A14

Fig. 14

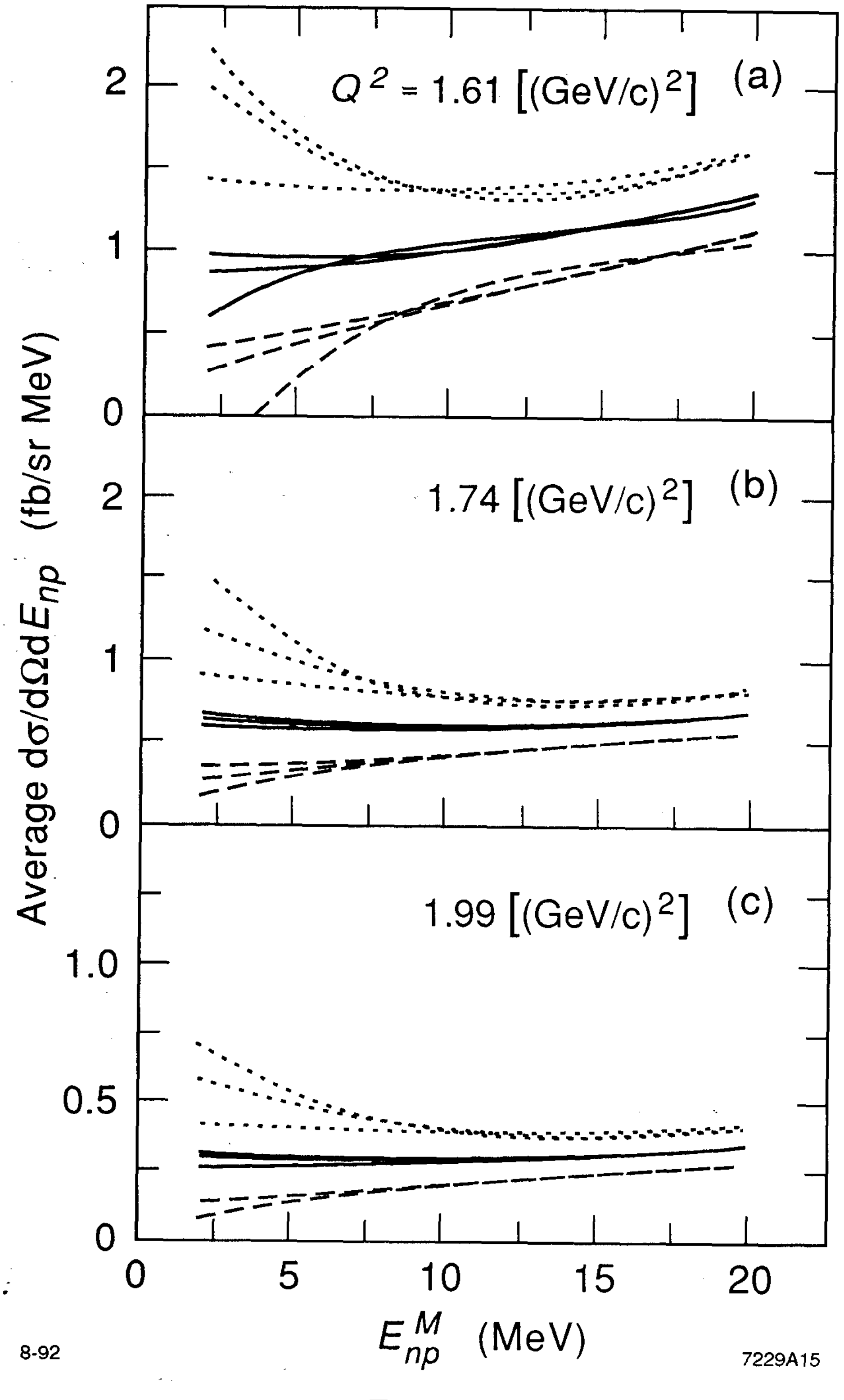

$Q^2 = 1.61$ [(GeV/c)^2] (a)
1.74 [(GeV/c)^2] (b)
1.99 [(GeV/c)^2] (c)
Average $d\sigma/d\Omega dE_{np}$ (fb/sr MeV)
2
1
0
1.0
0.5
0
5
10
15
20
E_{np}^{M} (MeV)
8-92
7229A15

Fig. 15

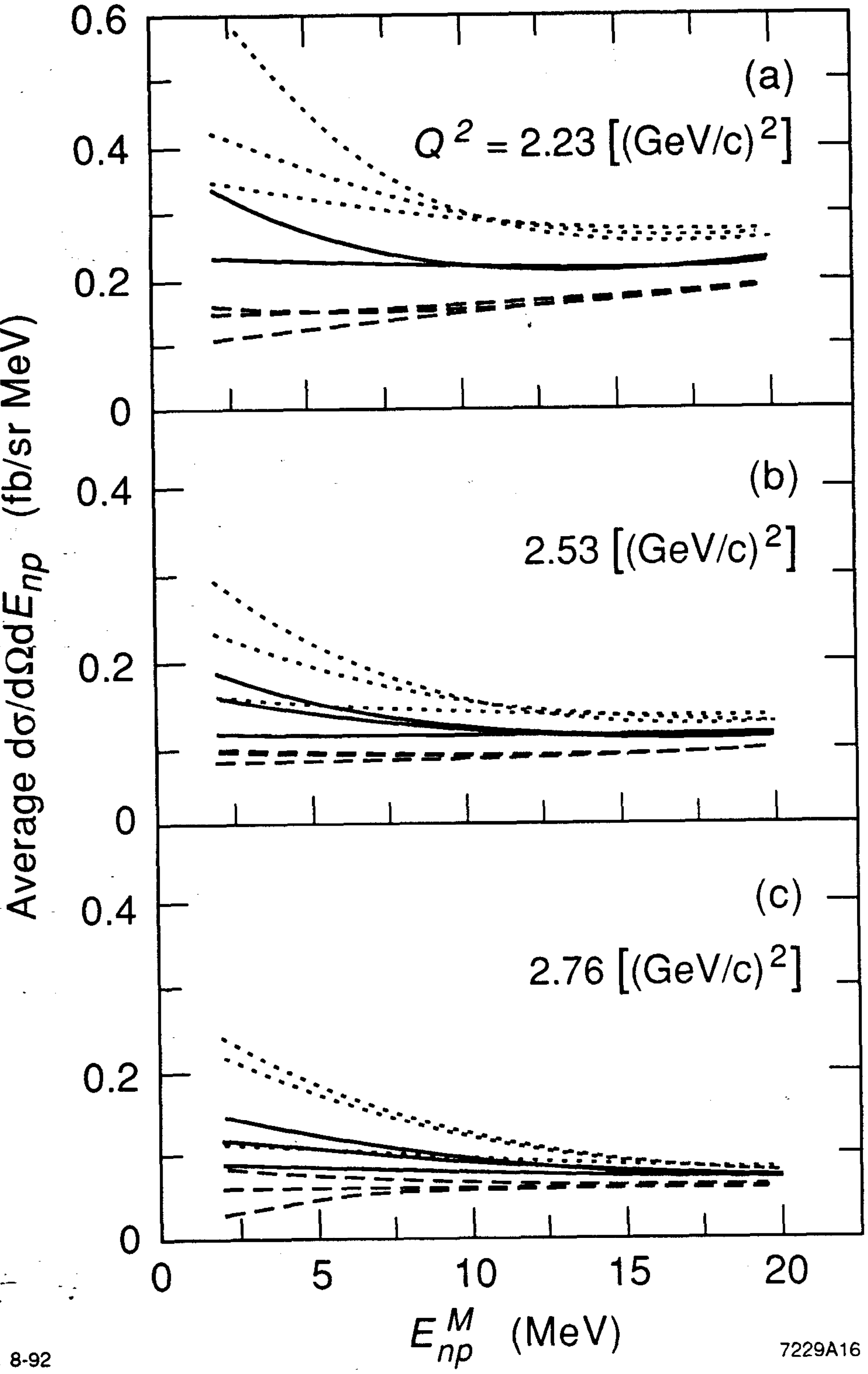
0.6
0.4
0.2
0
(a)
Q^2 = 2.23 [(GeV/c)^2]
(b)
2.53 [(GeV/c)^2]
(c)
2.76 [(GeV/c)^2]
Average $d\sigma/d\Omega dE_{np}$ (fb/sr MeV)
0
5
10
15
20
E_{np}^M (MeV)
8-92
7229A16

Fig. 16

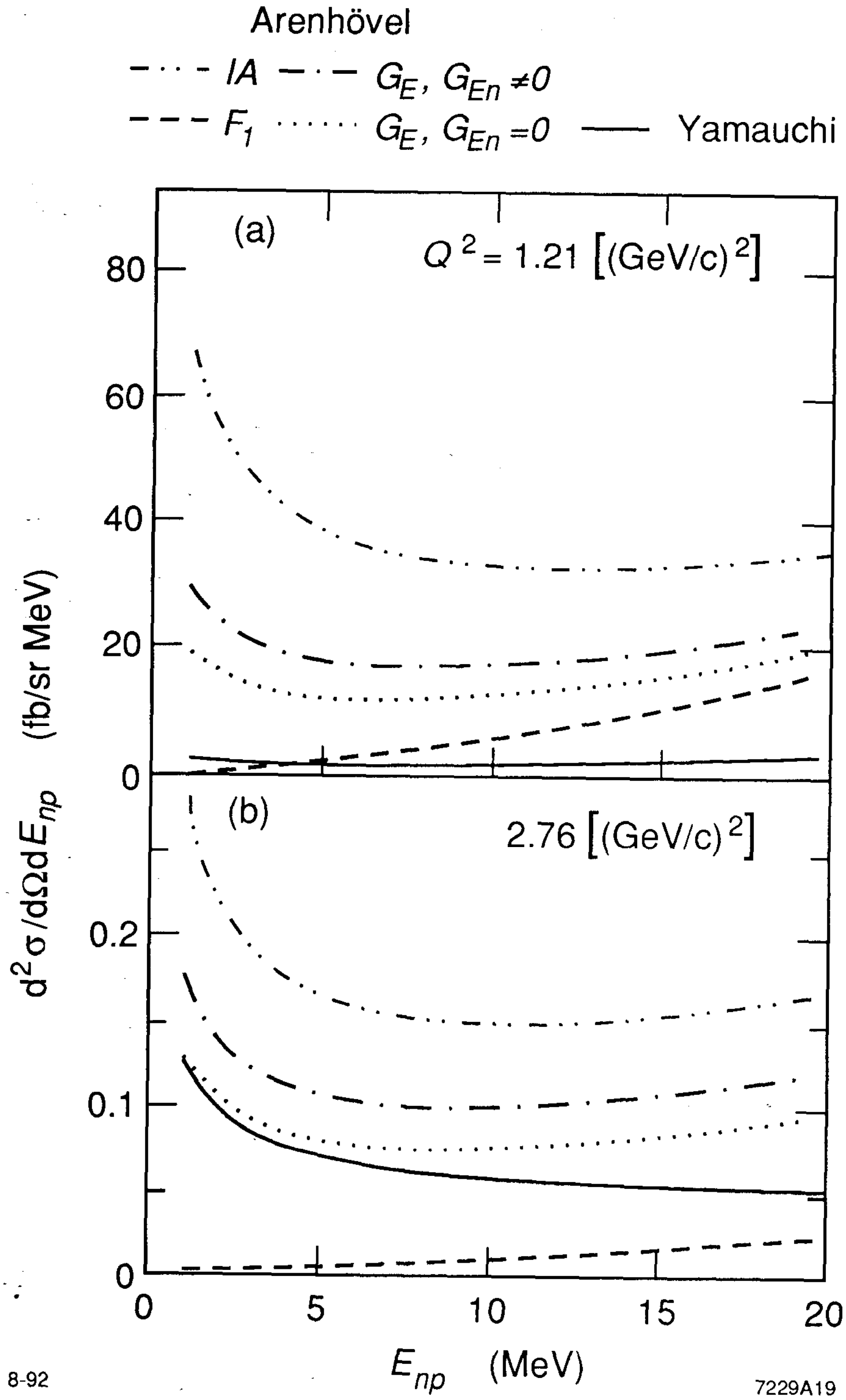
Arenhövel
IA
$G_E, G_{En} \neq 0$
F_1
$G_E, G_{En} = 0$
Yamauchi
(a)
$Q^2 = 1.21$ [(GeV/c)^2]
80
60
40
20
0
(b)
2.76 [(GeV/c)^2]
0.2
0.1
0
$d^2\sigma/d\Omega dE_{np}$ (fb/sr MeV)
0
5
10
15
20
E_{np} (MeV)
8-92
7229A19

Fig. 17

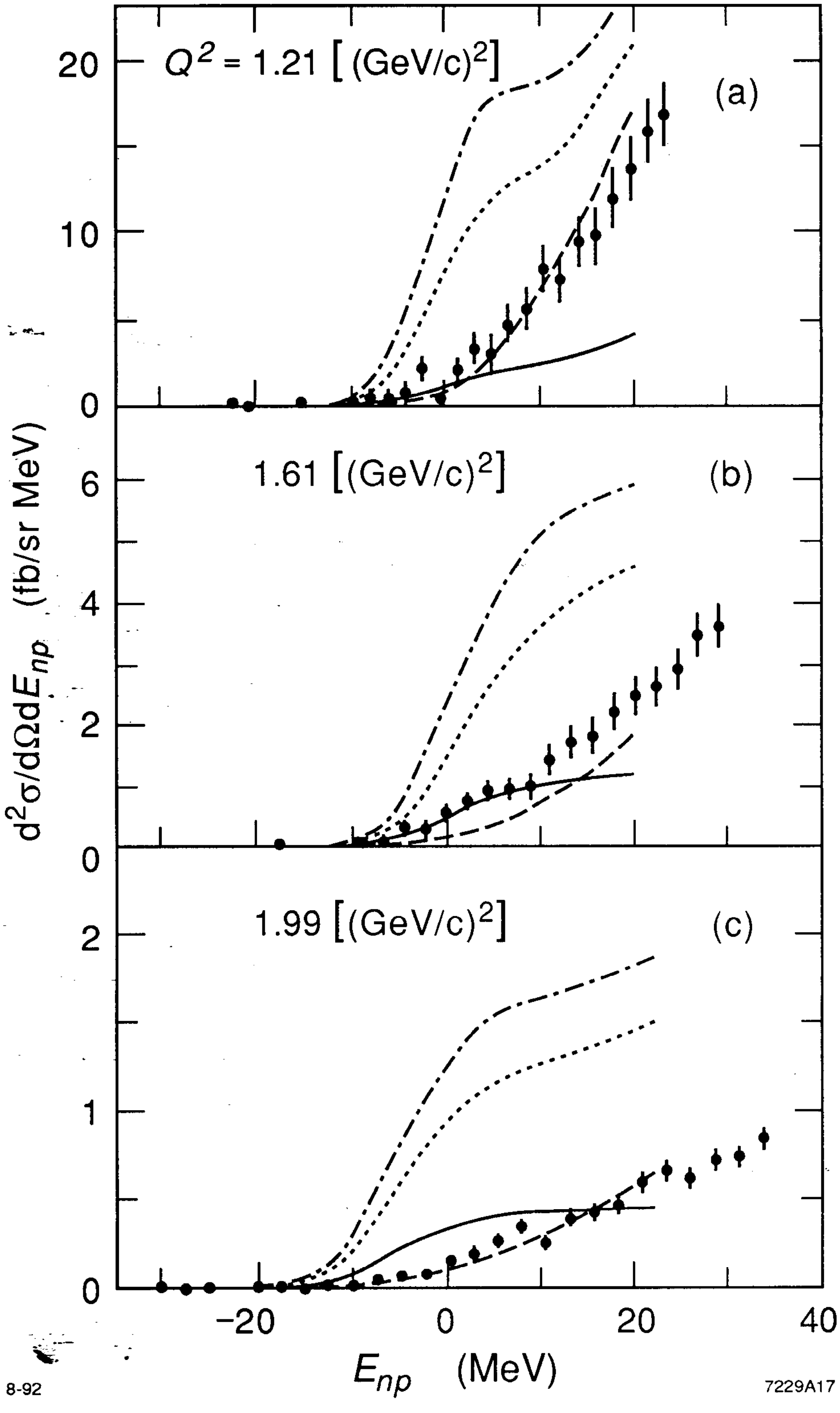

$Q^2 = 1.21$ [(GeV/c)^2]
(a)
1.61 [(GeV/c)^2]
(b)
1.99 [(GeV/c)^2]
(c)
$d^2\sigma/d\Omega dE_{np}$ (fb/sr MeV)
20
10
0
6
4
2
0
2
1
0
−20
0
20
40
E_{np} (MeV)
8-92
7229A17

Fig. 18

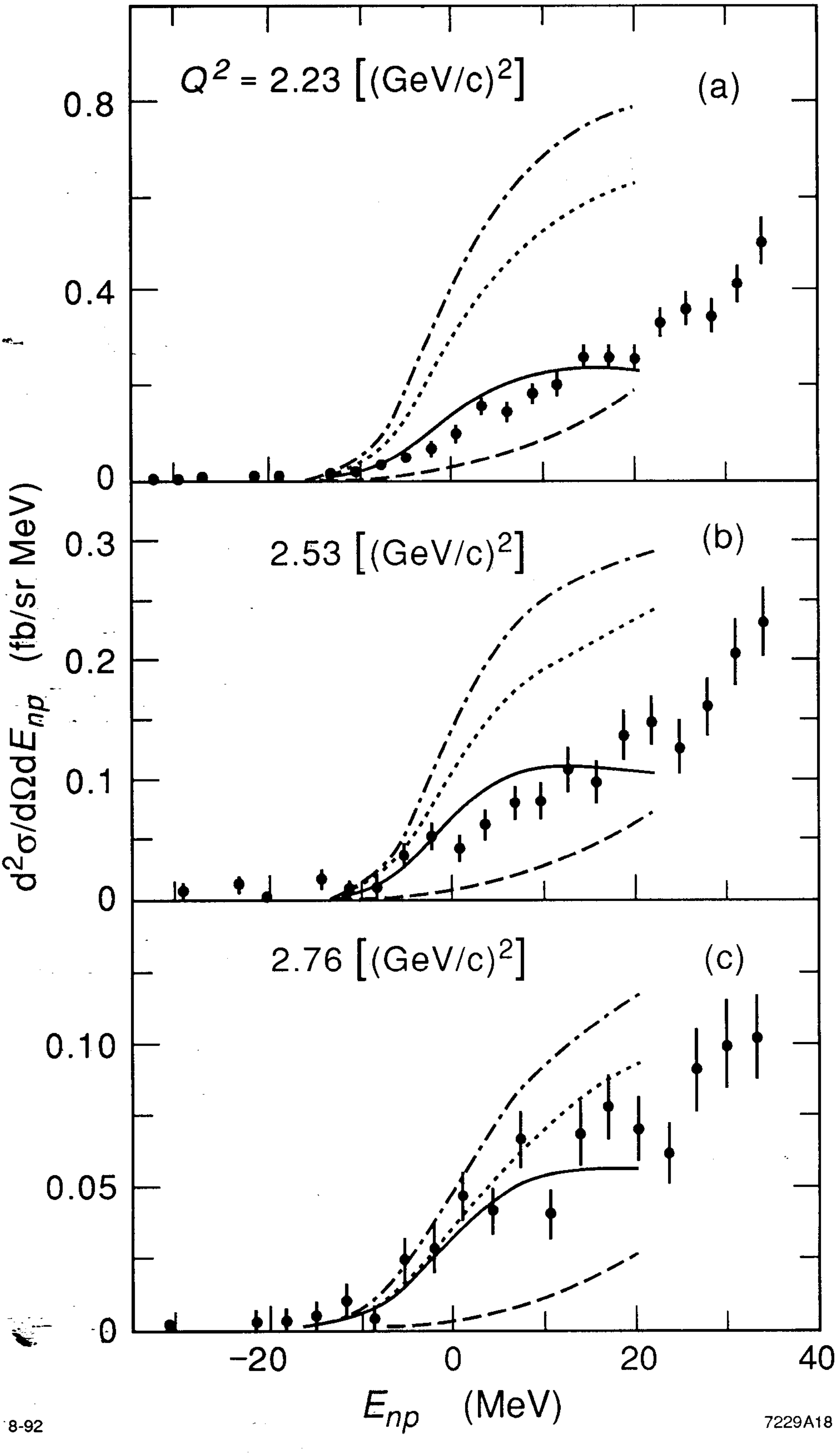
$Q^2 = 2.23$ [(GeV/c)^2]
(a)
0.8
0.4
0
2.53 [(GeV/c)^2]
(b)
0.3
0.2
0.1
0
2.76 [(GeV/c)^2]
(c)
0.10
0.05
0
−20
0
20
40
$d^2\sigma/d\Omega dE_{np}$ (fb/sr MeV)
E_{np} (MeV)
8-92
7229A18

Fig. 19

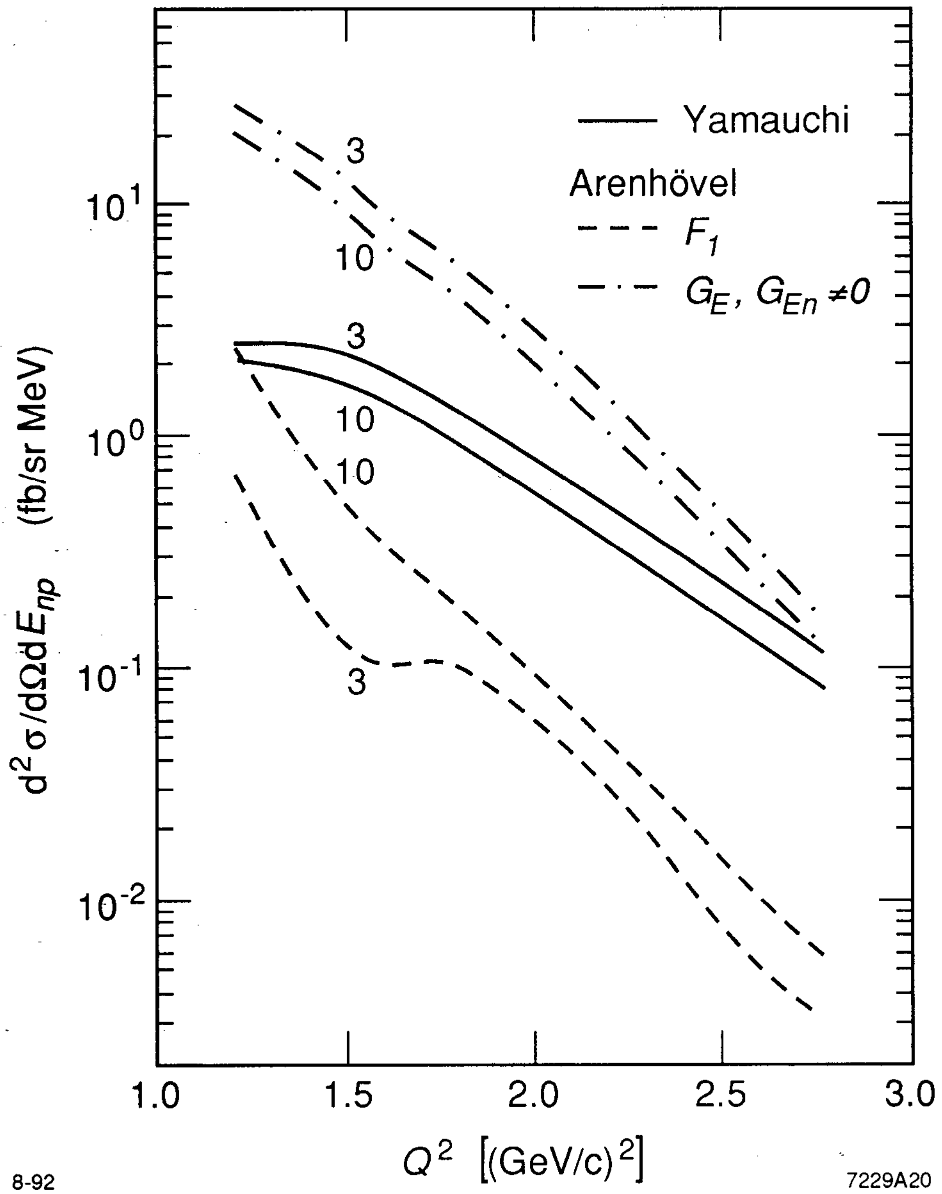
Yamauchi
Arenhövel
F_1
G_E, $G_{En} \neq 0$
3
10
3
10
10
3
10^1
10^0
10^{-1}
10^{-2}
$d^2\sigma/d\Omega dE_{np}$ (fb/sr MeV)
1.0
1.5
2.0
2.5
3.0
Q^2 [(GeV/c)^2]
8-92
7229A20

Fig. 20

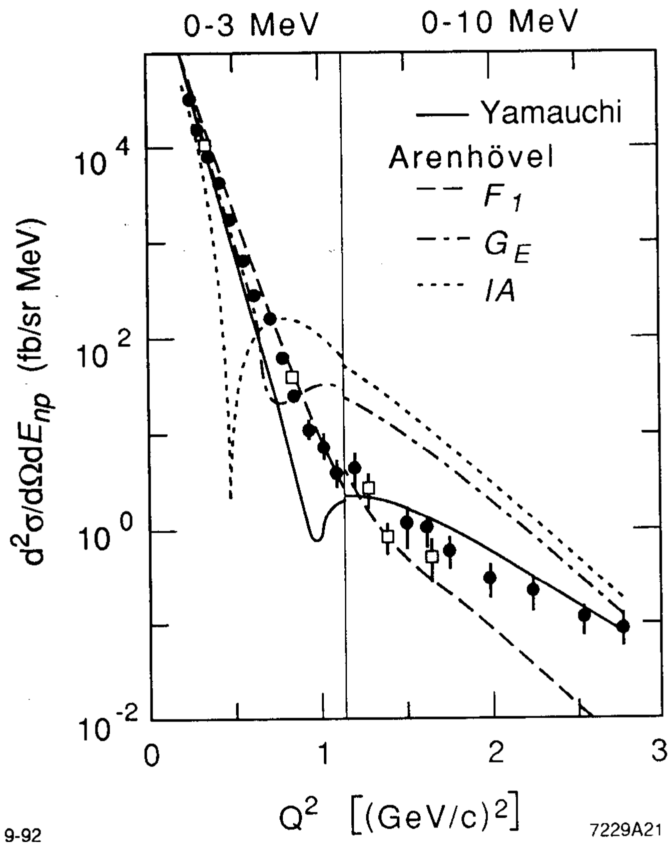
0-3 MeV
0-10 MeV
Yamauchi
Arenhövel
F_1
G_E
IA
10^4
10^2
10^0
10^{-2}
0
1
2
3
$d^2\sigma/d\Omega dE_{np}$ (fb/sr MeV)
Q^2 [(GeV/c)^2]
9-92
7229A21

Fig. 21

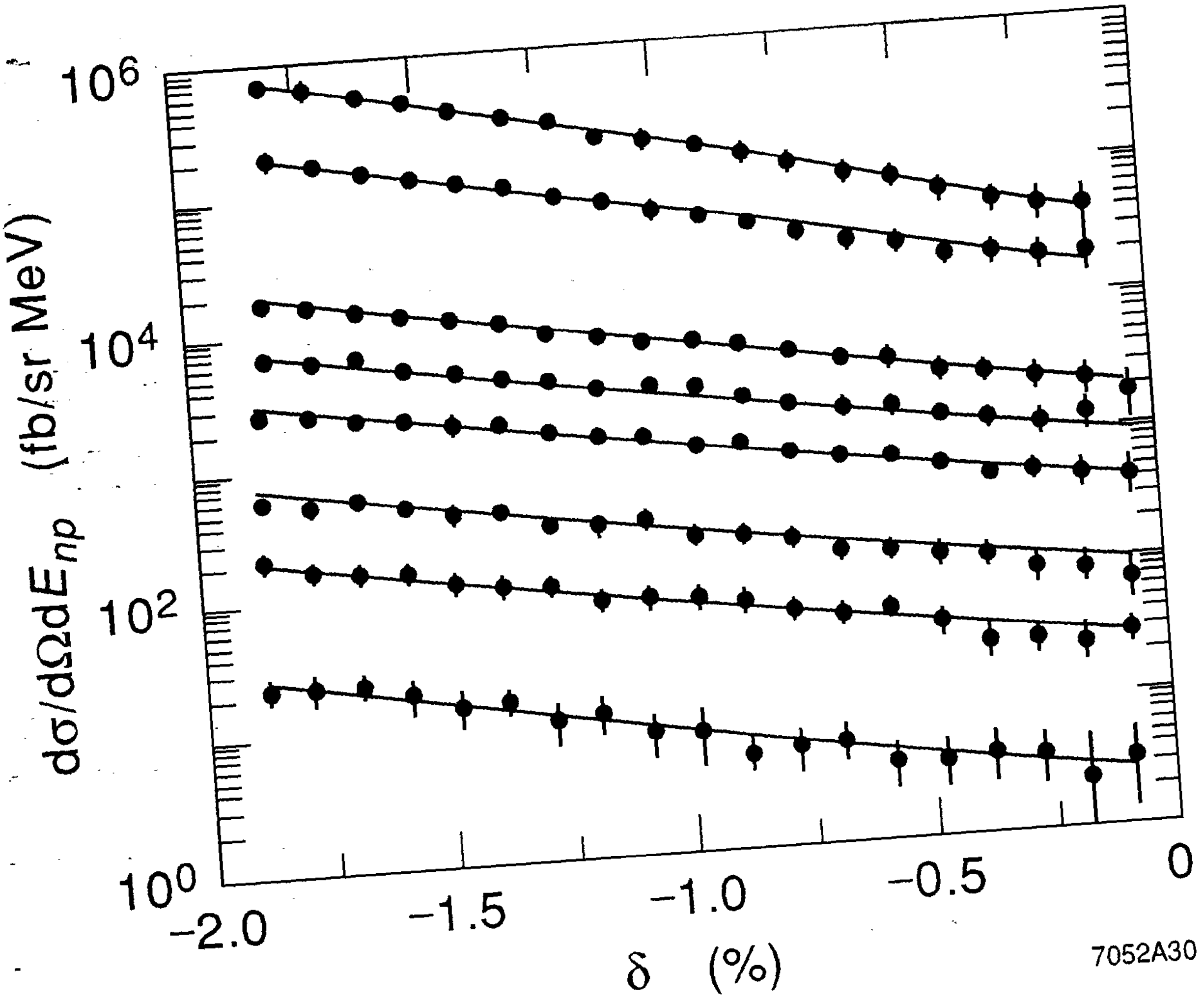

12–91

Fig. 22

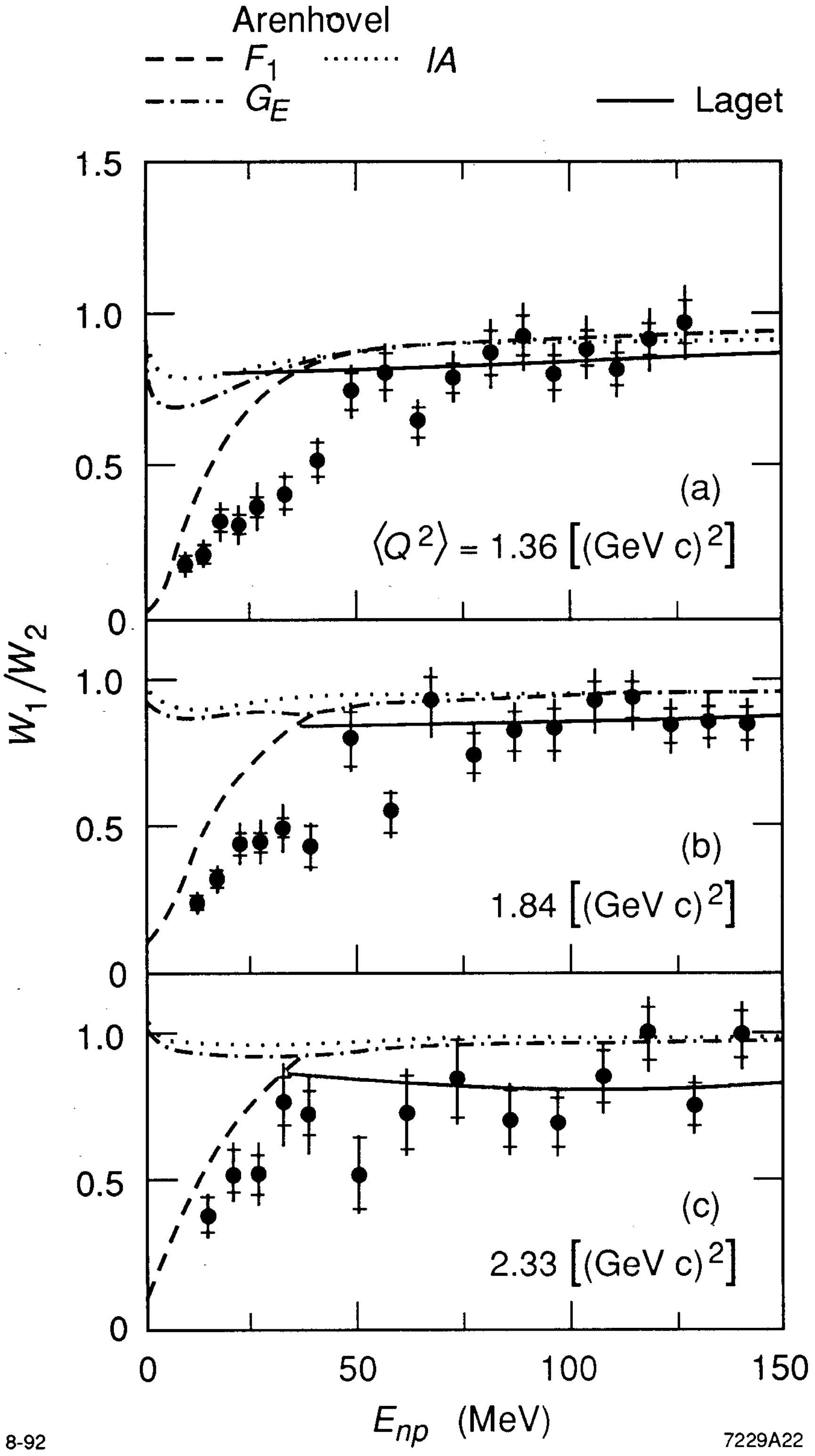

Arenhovel
F_1
IA
G_E
Laget
W_1/W_2
1.5
1.0
0.5
0
(a)
$\langle Q^2 \rangle = 1.36 \, [(\mathrm{GeV\,c})^2]$
(b)
$1.84 \, [(\mathrm{GeV\,c})^2]$
(c)
$2.33 \, [(\mathrm{GeV\,c})^2]$
0
50
100
150
E_{np} (MeV)
8-92
7229A22

Fig. 23